이학박사 학위논문

Fabrication of Electrode by Electrodeposition of Non-precious Catalyst and Their Applications to Solar-fuel Production

전기 도금을 이용한 비귀금속 기반의 전극 제작과 태양 연료 생산에의 응용

2016 년 8 월

서울대학교 대학원
화학부 전기분석화학전공
임 성 열

A Dissertation entitled

Fabrication of Electrode by Electrodeposition of Non-precious Catalyst and Their Applications to Solar-fuel Production

By Sung Yul Lim
Major: Electrochemistry

Submitted as partial fulfillment of the requirements for the Doctor of Philosophy degree in Chemistry

Advisor: Prof. Taek Dong Chung

Seoul National University
August, 2016

Abstract

The consumption of fossil fuels has adversely affected the environment, thereby resulting in a rapid increase in the global demand for investigating alternative sources of clean energy. One of the promising approaches for solving this issue is to convert solar energy into storable chemical fuels via photoelectrochemical reactions. Photoelectrochemical cell (PEC) is generally composed of several components, such as photoelectrodes, membrane separators, and catalysts; the development of efficient, economic, and robust catalysts is of great significance. Several studies on electrocatalysts have focused on the discovery of new electrocatalytic materials. Although active research for their commercialization is currently underway, development of electrocatalysts for commercialized solar-fuel production system still remains a challenge, attributed to the gap between performance and cost. Stepping back from the issues related to new material, this dissertation describes two examples of designing electrocatalysts using well-known materials by solution-processing methods, which are representative of low cost and scalability.

First, a light-guided electrodeposition technique was developed, which involves a method of directly patterning a

catalyst on amorphous Si (a-Si) by exploiting its photoconductive nature. A NiMo pattern, a well-known non-noble catalyst for hydrogen (H_2) evolution, was electrodeposited under the patterned illumination generated using a digital micromirror display (DMD) module. This process was completed in a single step without the use of any mask. Such patterned NiMo/SiO_x/a-Si photoelectrodes with sufficient catalyst loading exhibited a bare surface, which allows for light transmission, resulting in the intrinsic current density at 0 (V vs. RHE) and photovoltage of a-Si. Moreover, long-distance lateral electron transport between the adjacent NiMo catalyst patterns was observed.

Second, a biomimetic system for the PEC conversion of carbon dioxide (CO_2) to formate was developed, which represents one of the promising media H_2 storage in the future. The cathode at which the reduction of CO_2 occurs was prepared by the single-step electropolymerization of dopamine in the presence of formate dehydrogenase (FDH) as the biocatalyst, nicotinamide adenine dinucleotide (NADH) as the electron mediator between the underlying electrode and the reaction center in FDH. The cathode thus prepared was connected to cobalt phosphate (CoP_i)/bismuth vanadate ($BiVO_4$), which oxidizes water for producing oxygen (O_2) as the counter reaction to CO_2 reduction. Owing to the powerful

catalytic activity of FDH, PDA serving as the electronic wire, and, the $CoP_i/BiVO_4$ photoanode supplying sufficient photovoltage, the self-biased, prolonged conversion of CO_2 to foramte at zero voltage under simulated AM 1.5 illumination was possible.

Keywords: Photoelectrochemical cells, Catalyst, Light-guided electrodeposition, Hydrogen evolution, Carbon dioxide, Polydopamine, Electropolymerization

Student number: 2009-22918

Contents

List of Figures

2-6A).

[Fig. 2-8] Current-time curve recorded at -0.4 V (vs. Ag/AgCl) for 180 s. Red and gray lines represent the *i*-*t* curve in the presence and absence of Pt precursors in electrolyte solutions, respectively.

[Fig. 2-9] Effects of dynamic light pattern generated by 625 nm LED and DMD display on light-guided electrodeposition of Pt at -0.4 V (vs. Ag/AgCl) for 180 s. (A) Total charge passed during Pt electrodeposition under light with various diameters (Scale bar in inset images: 100 μm). The total charge was calculated by subtracting the integrated area of *i*-*t* curve in the absence of Pt precursors from in the presence of them. (B) Linear correlation between illuminated area and the size of pattern electrodeposited by light on a-Si (slope: 1.00 ± 0.02 and intercept: 0.044 ± 0.026 with an R^2 = 0.999). The diameters of the electrodeposited patterns were measured by the ImageJ program.

[Fig. 2-10] (A) Optical images of Pt spots electrodeposited by light (Scale bar: 400 μm). (B) Linear increase of total charge passed during electrodeposition of Pt with the number of light spots represented by the circle.

[Fig. 2-11] SEM image of the selected area marked in (as dotted rectangle in Fig 2-6B). Pt nanoparticles consisting of a line pattern are shown in the inset image. Dotted lines in

a-Si photocathode under light and dark conditions.

[Fig. 2-19] Schematic illustration of the HER operation mechanism at the NiMo pattern/SiO_x/a-Si photocathode.

[Fig. 2-20] Remote electrodeposition to investigate long-distance lateral electron transport in a-Si. (A) Optical images of light-guided Au electro-patterning 1.6 mm from the pre-patterned Pt line feature. (B) SEM images at each area marked on panel A.

[Fig. 2-21] EDS spectra of Pt, Au, and Au/Pt nanoparticles generated by electrodeposition as in Fig. 2-20. The Pt nanoparticles were deposited prior to Au electrodeposition and the Au particles electroplated on the illuminated area. Au/Pt represents the Au nanoparticles electrodeposited on the prepatterned Pt nanoparticles.

[Fig. 2-22] Current-ime (*i-t*) curves recorded during the Au electrodeposition in the absence and the presence of pre-patterned Pt. The inset shows a little hump (marked by the black dotted circle) at the initial stage.

[Fig. 2-23] Schematic illustration of long-distance lateral electron transport along the inversion layer in a-Si.

[Fig. 2-24] (A) SEM images of light-induced electrodeposited Pt line pattern obtained by scanning substrate under bias at −0.4 V (vs. Ag/AgCl). Substrates were moved at a rate of 1 μm s^{-1}. (B) and (C) show the area where the scanning starts and ends, respectively (scale

bar in A: 5 μm, B and C: 200 nm).

[Fig. 2-25] Local photocurrent in deaerated pH 4.5 buffer due to NiMo pattern. (A) Left: optical image of a line of electrodeposited NiMo. Right: scheme of local photocurrent measurement under 530 nm LED illumination generated by DMD (scale bar: 100 μm). (B) LSVs to probe local PEC activity as a function of illumination distance from the NiMo, which acts as an electron collector. LSVs under the same conditions without the NiMo pattern are presented for comparison.

[Fig. 2-26] Capacitance-voltage curves recorded for a SiO_x/a-Si photocathode under simulated AM 1.5 illumination and dark conditions measured at 100 Hz AC frequency.

[Fig. 2-27] (A) Optical image of the NiMo pattern/SiO_x/a-Si photocathode. (B) Linear sweep voltammograms for various spacings of NiMo dots of constant diameter, 400 μm. A spacing of 0 μm indicates the photocathode of non-patterned NiMo/SiO_x/a-Si.

[Fig. 2-28] Optimization of amount of NiMo catalyst for each spacing value on a-Si photocathode. (A) Current-time ($i-t$) curves for optimized light-guided electrodeposition of NiMo with various spacing. The results of LSV for different amounts of NiMo loaded, which were controlled by the number of reduction pulses. The spacing was varied at (B) 400, (C) 270, (D) 130, (E) 52, and (F) 0 μm under

simulated AM 1.5 illumination. The diameter of all NiMo dots was constant, 400 μm.

[Fig. 2-29] Histograms of the photocurrent at 0 V (vs. RHE) with various amounts of NiMo loading at each of the different spacings (Histogram colors correspond to the number of the potential pulses presented in panel B-E of Fig. 2-28).

[Fig. 2-30] Cross-sectional SEM images of NiMo films with different optimal amounts for different spacings. The optimized thicknesses were roughly (A) 150 nm, (B) 100 nm, (C) 80 nm, and (D) 50 nm (scale bar is 100 nm).

[Fig. 2-31] Variation in the total spectral reflectance of NiMo pattern/SiO_x/a-Si with spacing, in which the diameter of NiMo catalyst was constant, 400 μm. Here 0 μm refers to the a-Si substrate whose surface was fully covered with NiMo catalyst.

[Fig. 2-32] Linear sweep voltammograms for various spacing of NiMo dots under constant pattern diameter, 130 μm.

[Fig. 2-33] Linear sweep voltammograms for a variety of catalyst diameters with a constant spacing of 130 μm.

[Fig. 2-34] Calculation of ABPE.

[Fig. 2-35] HER performance for various D/S values at NiMo pattern/SiO_x/a-Si photocathodes from LSV. MPP denotes maximum power point.

[Fig. 2-36] IPCE measured using monochromatic light from a Xenon arc lamp and an applied bias of 0 V (vs. RHE). IPCE measurements were conducted at *D*/*S* of the 130/130 μm NiMo pattern/SiO_x/a-Si photocathode.

[Fig. 2-37] Stability test by chronoamperometry at a constant 0 V (vs. RHE) for 25 h. Durability measurements were conducted at *D*/*S* of the 130/130 μm of NiMo pattern/SiO_x/a-Si photocathode.

[Fig. 3-1] Schematic illustration of 3D structure and proposed formation mechanism of EC-PDA thin film-coated biocathode.

[Fig. 3-2] Optimization of photoanode. Current density (at 0.8 V vs. Ag/AgCl) of photoanodes as a function of the total charge passed during Bi electrodeposition onto the FTO electrode (blue) and the amounts of CoP_i loading (red) at the optimized $BiVO_4$ photoelectrode. The optimized total charge values for Bi and CoP_i deposition was 320 and 42.2 mC cm^{-2}, respectively.

[Fig. 3-3] Preparation procedure of CoP_i-electrodeposited $BiVO_4$ photoanode (CoP_i/$BiVO_4$).

[Fig. 3-4] Electrochemical fabrication procedure of Enzyme (E,FDH)/cofactor (C,NADH)-combined polydopamine (EC-PDA)-electropolymerized biocathode.

[Fig. 3-5] Electrochemical experiments demonstrating incorporating of FDH and NADH into the PDA layer during

electropolymerization. Cyclic voltammograms of a) DA only, b) FDH+DA, c) NADH+DA, and d) FDH+NADH+DA solutions (0.1 M sodium phosphate buffer, pH 6.0; scan rate 20 mV s^{-1}) to compare with voltammograms measured during DA electropolymerization.

[Fig. 3-6] Cyclic voltammograms of (A) NADH+DA and (B) FDH+DA solutions to compare with voltammograms measured during dopamime (DA) electropolymerization (0.1 M sodium phosphate buffer, pH 6.0; scan rate 20 mV s^{-1}). Electrochemical redox characteristics of NADH and FDH also shown in panel (A) and (B), respectively.

[Fig. 3-7] Reduction current with NAD^+ at bare GCE (0.1 M sodium phosphate, pH 7.0).

[Fig. 3-8] (A) Reduction currents with 1 mM NAD^+ at bare GCE and PDA-coated GCE (0.1 M sodium phosphate, pH 7.0). (B) The regeneration yields of NADH by bare and PDA-coated electrode were determined after 1 h reaction. A potential of -0.8 V (vs. Ag/AgCl) was applied in 0.1 M sodium phosphate buffer (pH 7.0) with 1 mM NAD^+.

[Fig. 3-9] Current density during the electrochemical polymerization of the PDA and EC-PDA layer (at 0.5 V vs Ag/AgCl).

[Fig. 3-10] Cyclic voltammograms of PDA and EC-PDA coated GCE in 0.1 M sodium phosphate buffer (pH 7.0; scan rate 25 mV s^{-1}).

Measurements were performed in 0.1 M sodium phosphate (pH 7.0) solution under CO_2 atmosphere at −0.5 V versus Ag/AgCl.

[Fig. 3-19] The top and cross-sectional view of $CoP_i/BiVO_4$ photoanode at the SEM images.

[Fig. 3-20] X-ray diffraction pattern of the $BiVO_4$ coated FTO electrode.

[Fig. 3-21] Mott-Schottky plot of bare $BiVO_4$ measured in 0.1 M sodium phosphate buffer (pH 7.0) containing 1 M sulfite ions as a sacrificial reagent at an applied frequency of 500, 750, and 1000 Hz.

[Fig. 3-22] Linear sweep voltammograms (scan rate 25 mV s^{-1}) of bare $BiVO_4$ and $CoP_i/BiVO_4$ on FTO electrodes under visible light irradiation using a 150 W Xe Arc lamp (light intensity adjusted to 100 mW cm^{-2}) equipped with cut-off filter at $\lambda > 420$ nm) in 0.1 M sodium phosphate buffer (pH 7.0).

[Fig. 3-23] Illustration of the functional processes underlying light-driven CO_2 reduction scheme.

[Fig. 3-24] Schematic representation of the photochemical system for the reduction of CO_2 to formate utilizing a $CoP_i/BiVO_4$ photoanode and EC-PDA biocathode working under visible light irradiation.

[Fig. 3-25] Linear sweep voltammogram of photoelectrochemical CO_2 reduction at two-electrode

configuration as shown in Fig. 3-24 (scan rate 25 mV s^{-1}).

[Fig. 3-26] Photocatalytic formate formation from CO_2 gas as a function of irradiation time. CO_2 reduction was performed using a two-electrode configuration with no external bias (at 0 V vs photoanode) in 0.1 M sodium phosphate (pH 7.0). The irradiation area was 1.7 cm^2 (Inset: chronoamperometry profile for 24 h).

[Fig. 3-27] Photograph of the photoelectrochemical system for the reduction of CO_2 to formate. The combination of a $CoP_i/BiVO_4$ photoanode and an EC-PDA biocathode functioning under visible light irradiation.

1. Introduction

1.1 Background and Overview

Energy is essential to our modern life. Thus far, fossil fuels such as coal, oil, and natural gas have been used as primary sources of energy. Securing a robust supply of petroleum primarily resulted in the leap into the ranks of developed nations. On the other hand, with increase in both population and income, energy use also increases. Since the 1990s, the demand for energy has grown by greater than 50% [1], with fossil fuels still providing 87% [2] of the energy that we use. Nevertheless, because of the limited resources of fossil fuels, the sustainability of energy is currently one of the major concerns in terms of its availability relative to its rate of consumption. In addition, side products arising from the combustion of fossil fuels cause environmental pollution. Moreover, in some areas, global warming directly threatens animals and plants. All of these issues caused by fossil fuels have currently spurred the transformation of energy systems to eco-friendly, renewable energy.

Several studies, as well as efforts, have been focused on the utilization of solar energy [3-13], one of the several candidates available as a renewable energy resource,

attributed to its unmatched resource potential. In fact, only 0.01% of the solar energy reaching the Earth's surface is sufficient to deal with global energy consumption [14]. One of the approaches involves the development of photovoltaics (PVs) for the production of solar electricity [15]; PVs involve the direct conversion of sunlight into electricity or heat. Owing to extensive efforts focused on PVs during the past decade, significant progress has been achieved. Even though the cost of solar cell panels has rapidly declined, deployment for commercialization is achieved and the energy payback period is now decreased to less than 2.5 years by the use of Si-based PVs having higher than 20% efficiency [1], researches for higher efficiency and lower cost-solar cells are still ongoing to overcome the fundamental drawbacks that still needs to be addressed. Because of the temporal variation of sunlight illumination and volatile nature of electricity, solar fuel generation has gained significant interests [16-20]. As compared to solar electricity systems, solar fuel can directly provide storable final fuel by utilizing solar energy. Unlike the generation of solar electricity, solar fuel production systems are typically implemented in liquid environments [14]. Solar fuel systems can be categorized into four types, molecular systems, inorganic particles, semiconductor photoelectrodes, and photovoltaic electrolysis [14,21,22]. However, as compared with the

commercialization of solar electricity systems, that of fuel systems is significantly more challenging in terms of the development of efficient, safe, cost-effective and durable devices [1,14,21].

On the other hand, three primary targets-hydrogen, hydrocarbons, and ammonia-are attracting attention for use as solar fuels [14]. Typically, hydrogen (H_2) is produced by the photoelectrolysis of water. Although the gaseous products thus obtained are highly explosive, H_2 and oxygen (O_2), which represent the fuel and by-product from the counter reaction, respectively, a thermodynamic energy (1.23 V) [23] relatively lower than that of any other reaction, as well as a liquid form of reactants, are advantageous for water splitting. Hydrocarbons, methane, or formate obtained from the hydrogenation of CO_2, which represents a simple means for storage and distribution, can also be implemented [14]. Such hydrocarbons exhibit energy density greater than H_2 and are present in a liquid form, which is required for transportation and storage [14,24]. However, the reduction of CO_2 producing hydrocarbons is highly endothermic and requires a large overpotential of at least 800 mV, attributed to the large reorganization energy [25,26]. In addition, CO_2 exhibits low solubility in an aqueous electrolyte [27-29], which is one of the most eco-friendly solvents; hence, it is difficult to achieve a high Faradaic and energy efficiency.

Besides H_2 and hydrocarbons, ammonia is another high-energy-density fuel, produced by the utilization of nitrogen (N_2) [11,14]; N_2 is the most abundant constituent in air. However, because of the unmatched high input energy, such as overpotential, studies for acquiring ammonia are relatively scarce as compared with the two aforementioned cases [11,14].

Typically, solar fuel generation systems are based on photoelectrochemical (PEC) cells as they mimic artificial photosynthetic systems [21,30]. PEC cells consist of three components, which is semiconductor, membrane separator, and catalyst. Semiconductor serves as a light absorber that generates charge carriers. After generation of electron/hole pairs, the separation of charge carriers is facilitated by an electric field gradient in the semiconductor electrode. The photogenerated charge carriers transported to the semiconductor/liquid interface are transferred to the electrolyte solutions, thereby inducing half-reactions of interest. A membrane prevents the continuous decrease of device performance by separating products from the cathode and anode. However, the intrinsic surface of semiconductor usually exhibits low reactivity to advance (electro)chemical reactions [31-33]. Thus, catalyst is required to assist charge transfer to electrolyte by decreasing kinetic overpotentials.

The main research stream has been focused on the development of new materials as durable, efficient, safe, and cost-effective components of PEC cells [1,14,21]. For semiconductor electrodes, several classes of light absorbers have been explored, *e.g.* Si-based photoelectrodes, group Ⅲ-Ⅴ semiconductors, metal oxides, chalcogenides, and chalcopyrites [34-37]. Although numerous studies related to the examination of hundreds of catalysts have been reported with different compositions and structures fabricated by various methods, Pt group catalysts are still the optimum materials for solar energy conversion reactions [21]. Nevertheless, these catalysts suffer from crucial drawbacks of high cost and price instability, which hinder their commercialization for water electrolysis [14]. In summary, the commercialization of integrated solar fuel production systems has not been reported [1,14].

The primary goal of this dissertation is to fabricate electrodes for solar fuel systems via the electrodeposition of non-precious catalysts. Electrodeposition is a solution-processing method, which is well known to be a cost-effective technology with scalability and promptness [38-40]. Hence, several studies on the electrodeposition of non-noble catalysts for energy conversion reactions have been conducted thus far [33,41-43]. Several electrodeposited catalysts for hydrogen evolution reaction

(HER) were developed, such as Co [44], CoMo [45], CoNiFe [46], Fe [47], FeMo [48], MoS [49], Ni [47], NiFe [47], NiMo [45,50], NiMoCo [51], and NiMoFe [52]. In addition, Co [53], Co/B [54], Co/P [55], CoFe, Cu, Fe, FeMn [53], Ni [56], Ni/B [57], NiCo [56], NiFe [53], and NiMoFe [58] are effective in oxygen evolution reaction (OER). Pb [59], SnPb [60], Sn [61], Cu [62,63], CuPd [64], CuSn [65], Bi [28], and Zn [66] were electrodeposited and investigated as catalysts for electrochemical reduction of CO_2.

Stepping back from the issues related to the development of new materials, this dissertation discusses the efforts focused on the fabrication and design of electrodes by recombining well-known catalyst materials with electrodeposition. This thesis is divided into two main chapters. In **Chapter 2**, a light-guided electrodeposition method is reported, which can form a NiMo pattern on amorphous silicon (a-Si) in a single step by exploiting its photoconductive nature [67]. The patterned NiMo on the a-Si photocathode exhibits an intrinsic saturated current density and onset potential for HER, permitting light transmission via the bare surface, as well as sufficient catalyst loading. In addition, long-distance lateral electron transport, as reported in crystalline Si through an inversion channel is also investigated. **Chapter 3** discusses the

fabrication of thin film bioelectrodes, composed of polydopamine (PDA), formate dehydrogenase (FDH), and nicotinamide adenine dinucleotide (NADH) for the conversion of CO_2 to formate in single-step electrodeposition [68]. Owing to the tightly bound NADH and FDH on the PDA film, this artificial bioelectrode exhibits comparatively low overpotentials, high Faradaic efficiency and unexpected long-term stability. Furthermore, by mimicking photosynthesis, the production of formate from CO_2 occurs at zero voltage via the combination of a cobalt phosphate/bismuth vanadate ($CoP_i/BiVO_4$) photoanode. Finally, Chapter 4 summarizes the conclusion and contributions of this study.

1.2 References

[1] N. S. Lewis, *Science*, 2016, *351*, 353.

[2] *BP Statistical Review of World Energy*, 2013.

[3] X.-l. Meng, N. Sellami, A. R. Knox, A. Montecucco, J. Siviter, P. Mullen, A. Ashraf, A. Samarelli, L. F. Llin, D. J. Paul, W.-g. Li, M. C. Paul, D. H. Gregory, G. Han, M. Gao, T. Sweet, R. Freer, F. Azough, R. Lowndes, X.-l. Xia and T. K. Mallick, *Energ. Convers. Manage.*, 2016, *114*, 142.

[4] A. G. Scheuermann, J. P. Lawrence, K. W. Kemp, T. Ito, A. Walsh, C. E. D. Chidsey, P. K. Hurley and P. C. McIntyre, *Nat. Mater.*, 2016, *15*, 99.

[5] J. Luo, J.-H. Im, M. T. Mayer, M. Schreier, M. K. Nazeeruddin, N.-G. Park, S. D. Tilley, H. J. Fan and M. Graetzel, *Science*, 2014, *345*, 1593.

[6] D. V. Esposito, I. Levin, T. P. Moffat and A. A. Talin, *Nat. Mater.*, 2013, *12*, 562.

[7] J. Oh, H.-C. Yuan and H. M. Branz, *Nat. Nanotechnol.*, 2012, *7*, 743.

[8] K. Jin, J. Park, J. Lee, K. D. Yang, G. K. Pradhan, U. Sim, D. Jeong, H. L. Jang, S. Park, D. Kim, N.-E. Sung, S. H. Kim, S. Han and K. T. Nam, *J. Am. Chem. Soc.*, 2014, *136*, 7435.

[9] J. Kye, M. Shin, B. Lim, J.-W. Jang, I. Oh and S. Hwang, *ACS Nano*, 2013, *7*, 6017.

[10] C. Liu, J. J. Gallagher, K. K. Sakimoto, E. M. Nichols, C. J. Chang, M. C. Y. Chang and P. Yang, *Nano Lett.*, 2015, *15*, 3634.

[11] Y. Abghoui, A. L. Garden, V. F. Hlynsson, S. Bjorgvinsdottir, H. Olafsdottir and E. Skulason, *Physi. Chem. Chem. Phys.*, 2015, *17*, 49098.

[12] M. A. Green, *Prog. Photov.*, 2009, *17*, 183.

[13] J. Jean, P. R. Brown, R. L. Jaffe, T. Buonassisi and V. Bulovic, *Energy Environ. Sci.*, 2015, *8*, 1200.

[14] S. Dahl and I. Chorkendorff, *Nat. Mater.*, 2012, *11*, 1001.

[15] C. Zheng and D. M. Kammen, *Energy Policy*, 2014, *67*, 159.

[16] P. Yang and J.-M. Tarascon, *Nat. Mater.*, 2012, *11*, 560.

[17] J. Newman, P. G. Hoertz, C. A. Bonino and J. A. Trainham, *J. Electrochem. Soc.*, 2012, *159*, A1722.

[18] I. Thomann, B. A. Pinaud, Z. Chen, B. M. Clemens, T. F. Jaramillo and M. L. Brongersma, *Nano Lett.*, 2011, *11*, 3440.

[19] C. Ampelli, G. Centi, R. Passalacqua and S. Perathoner, *Energy Environ. Sci.*, 2010, *3*, 292.

[20] J. A. Herron, J. Kim, A. A. Upadhye, G. W. Huber and C. T. Maravelias, *Energy Environ. Sci.*, 2015, *8*, 126.

[21] J. R. McKone, N. S. Lewis and H. B. Gray, *Chem.*

Mater., 2014, *26*, 407.

[22] A. C. Nielander, M. R. Shaner, K. M. Papadantonakis, S. A. Francis and N. S. Lewis, *Energy Environ. Sci.*, 2015, *8*, 16.

[23] Z. Chen, T. F. Jaramillo, T. G. Deutsch, A. Kleiman-Shwarsctein, A. J. Forman, N. Gaillard, R. Garland, K. Takanabe, C. Heske, M. Sunkara, E. W. McFarland, K. Domen, E. L. Miller, J. A. Turner and H. N. Dinh, *J. Mater. Res.*, 2010, *25*, 3.

[24] S. Lin, C. S. Diercks, Y.-B. Zhang, N. Kornienko, E. M. Nichols, Y. Zhao, A. R. Paris, D. Kim, P. Yang, O. M. Yaghi and C. J. Chang, *Science*, 2015, *349*, 1208.

[25] C. Costentin, M. Robert and J.-M. Saveant, *Chem. Soc. Rev.*, 2013, *42*, 2423.

[26] J. Qiao, Y. Liu, F. Hong and J. Zhang, *CChem. Soc. Rev.*, 2014, *43*, 631.

[27] C. Costentin, S. Drouet, M. Robert and J.-M. Saveant, *Science*, 2012, *338*, 90.

[28] J. Medina-Ramos, J. L. DiMeglio and J. Rosenthal, *J. Am. Chem. Soc.*, 2014, *136*, 8361.

[29] B. A. Rosen, A. Salehi-Khojin, M. R. Thorson, W. Zhu, D. T. Whipple, P. J. A. Kenis and R. I. Masel, *Science*, 2011, *334*, 643.

[30] X. Ding, Y. Gao, L. Zhang, Z. Yu, J. Liu and L. Sun, *Electrochim. Acta.*, 2014, *149*, 337.

[31] P. Dai, J. Xie, M. T. Mayer, X. Yang, J. Zhan and D. Wang, *Angew. Chem., Int. Ed.*, 2013, *52*, 11119.

[32] C. C. L. McCrory, S. Jung, I. M. Ferrer, S. M. Chatman, J. C. Peters and T. F. Jaramillo, *J. Am. Chem. Soc.*, 2015, *137*, 4347.

[33] C. C. L. McCrory, S. Jung, J. C. Peters and T. F. Jaramillo, *J. Am. Chem. Soc.*, 2013, *135*, 16977.

[34] D. V. Esposito, J. B. Baxter, J. John, N. S. Lewis, T. P. Moffat, T. Ogitsu, G. D. O'Neil, P. Tuan Anh, A. A. Talin, J. M. Velazquez and B. C. Wood, *Energy Environ. Sci.*, 2015, *8*, 2863.

[35] A. Kudo and Y. Miseki, *Chem. Soc. Rev.*, 2009, *38*, 253.

[36] E. L. Miller, N. Gaillard, J. Kaneshiro, A. DeAngelis and R. Garland, *Int. J. Energ. Res.*, 2010, *34*, 1215.

[37] X. Chen, S. Shen, L. Guo and S. S. Mao, *Chem. Rev.*, 2010, *110*, 6503.

[38] Y. Liu, D. Gokcen, U. Bertocci and T. P. Moffat, *Science*, 2012, *338*, 1327.

[39] A. Sang Hyun, H. Tan, M. Haensch, Y. Liu, L. A. Bendersky and T. P. Moffat, *Energy Environ. Sci.*, 2015, *8*, 3557.

[40] P. V. Dudin, M. E. Snowden, J. V. Macpherson and P. R. Unwin, *ACS Nano*, 2011, *5*, 10017.

[41] C. G. Morales-Guio, S. D. Tilley, H. Vrubel, M.

Graetzel and X. Hu, *Nat. Commun.*, **2014**, 5.

[42] J. R. McKone, E. L. Warren, M. J. Bierman, S. W. Boettcher, B. S. Brunschwig, N. S. Lewis and H. B. Gray, *Energy Environ. Sci.*, **2011**, *4*, 3573.

[43] J. C. Hill, A. T. Landers and J. A. Switzer, *Nat. Mater.*, **2015**, *14*, 1150.

[44] O. Savadogo and H. Lavoie, *Int. J. Hydrogen Energy*, **1992**, *17*, 473.

[45] C. L. Fan, D. L. Piron, A. Sleb and P. Paradis, *J. Electrochem. Soc.*, **1994**, *141*, 382.

[46] M. Jafarian, O. Azizi, F. Gobal and M. G. Mahjani, *Int. J. Hydrogen Energy*, **2007**, *32*, 1686.

[47] R. Solmaz and G. Kardas, *Electrochim. Acta*, 2009, **54**, 3726.

[48] N. R. Elezovic, V. D. Jovic and N. V. Krstajic, *Electrochim. Acta*, **2005**, *50*, 5594.

[49] D. Merki, S. Fierro, H. Vrubel and X. Hu, *Chemical Science*, **2011**, *2*, 1262.

[50] N. V. Krstajic, V. D. Jovic, L. Gajic-Krstajic, B. M. Jovic, A. L. Antozzi and G. N. Martelli, *Int. J. Hydrogen Energy*, **2008**, *33*, 3676.

[51] C. L. Fan, D. L. Piron and P. Paradis, *Electrochim. Acta*, **1994**, *39*, 2715.

[52] I. A. Raj and K. I. Vasu, *J. Appl. Electrochem.*, **1992**, *22*, 471.

[53] M. D. Merrill and R. C. Dougherty, *J. Phys. Chem. C*, 2008, *112*, 3655.

[54] Y. Surendranath, M. Dinca and D. G. Nocera, *J. Am. Chem. Soc.*, 2009, *131*, 26150.

[55] M. W. Kanan and D. G. Nocera, *Science*, 2008, *321*, 1072.

[56] D. A. Corrigan and R. M. Bendert, *J. Electrochem. Soc.*, 1989, *136*, 723.

[57] M. Dinca, Y. Surendranath and D. G. Nocera, *Proc. Natl. Acad. Sci. U. S. A.*, 2010, *107*, 10337.

[58] M. Jayalakshmi, W.-Y. Kim, K.-D. Jung and O.-S. Joo, *Int. J. Electrochem. Sci.*, 2008, *3*, 908.

[59] J. Wang, H. Wang, Z. Han and J. Han, *Front. Chem. Sci. Eng.*, 2015, *9*, 57.

[60] S. Y. Choi, S. K. Jeong, H. J. Kim, I.-H. Baek and K. T. Park, *ACS Sustainable Chem. Eng.*, 2016, *4*, 1311.

[61] Y. Chen and M. W. Kanan, *J. Am. Chem. Soc.*, 2012, *134*, 1986.

[62] G. Keerthiga, B. Viswanathan and R. Chetty, *Catal. Today*, 2015, *245*, 68.

[63] R. Kas, R. Kortlever, A. Milbrat, M. T. M. Koper, G. Mul and J. Baltrusaitis, *Phys. Chem. Chem. Phys.*, 2014, *16*, 12194.

[64] S. Zhang, P. Kang, M. Bakir, A. M. Lapides, C. J. Dares and T. J. Meyer, *Proc. Natl. Acad. Sci. U. S. A.*, 2015, *112*,

15809.

[65] A. T. G.-E. Saad Sarfraz, Abdesslem Jedidi, Luigi Cavallo, and Kazuhiro Takanabe, *ACS Catal.*, 2016, *6*, 2842.

[66] J. Rosen, G. S. Hutchings, Q. Lu, R. V. Forest, A. Moore and F. Jiao, *ACS Catal.*, 2015, *5*, 4586.

[67] S. Y. Lim, Y.-R. Kim, K. Ha, J.-K. Lee, J. G. Lee, W. Jang, J.-Y. Lee, J. H. Bae and T. D. Chung, *Energy Environ. Sci.*, 2015, *8*, 3654.

[68] S. Y. L. Soo Youn Lee, Daye Seo, Jin-Young Lee, and T. D. Chung, *Adv. Energy Mater.*, 2016, doi:10.1002/aenm.201502207.

2. Light-Guided Electrodeposition of Non-noble Catalyst Patterns for Photoelectrochemical Hydrogen Evolution

2.1 Introduction

Unremitting effort has continued since the pioneering work of Fujishima and Honda in 1972 [1], to produce storable chemical fuels, particularly hydrogen, more efficiently by photoelectrochemical (PEC) reactions. Recently, significant advances instability and efficiency were achieved by the metal-insulator-semiconductor (MIS)-based photoelectrode configuration [2-7]. Photo-generated electrons at the semiconductor penetrate the insulator and transfer to the metal layer, which should serve as an electrocatalyst for hydrogen evolution. However, MIS-based photoelectrodes, in practice, are facing difficulties of unsated photoelectrochemical performance and high cost. To date, considerable efforts for MIS photoelectrodes system have been made in developing "transparent catalysts" to permit the light transmission while maintaining the sufficient amount of catalyst loaded, which can be classified into five approaches [8-11]. The first approach involves the placement of transparent conducting oxide (TCO) beneath

the catalyst/insulator/semiconductor photoelectrodes and illumination from the back side through TCO [12]. This permits a wider range of materials to be used, including opaque catalysts, but the high expense of TCO must be addressed [13]. The second approach is to seek new electrocatalytic materials to replace noble metals. Reportedly, thin layers (monolayers to a few nanometers) of Pt do not severely interrupt light transmission and can exhibit sufficient catalytic performance in acidic condition [14–16]. The third approach is to massively load non-precious metal catalysts on to a large semiconductor surface area, despite the poor saturation current density [17–19]. The fourth approach is to utilize molecular catalysts. Due to the perfect transparency and ideal for chemical study of catalyst operation mechanism, much efforts have been made to design and synthesize new molecular electrocatalysts for hydrogen evolution (HER) [20–23]. Although several molecular HER catalysts show high turnover frequency, stability issue especially in aqueous conditions is still challenging [8,24]. The final approach employs patterned catalysts that leave bare surfaces between neighbouring electrodes for optical transmission. Such a surface is exposed to the solution as well as light. With an MIS photoelectrode based on crystalline Si (c-Si), this strategy has proven to be promising by recent works showing that

patterned Pt/Ti catalysts can bring about substantial enhancement in PEC activity for the HER [6,7].

Various methods have been proposed to fabricate patterned electrodes [25–30]. Most are template–assisted techniques based on typical photolithography, posing inherent limitations in terms of complexity, cost, and scalability. Electrodeposition is a relatively simple method that enables cost–effective formation of metal and semiconductor nanostructures with scalability [31–33]. Furthermore, the surface characteristics as well as the amount of electrodeposited materials can be varied through the nucleation process and growth rate by adjusting the magnitude and duration of the applied voltage or current pulses [34,35]. However, there is a critical prerequisite for spatial–selective electrodeposition to be a successful alternative to photolithography in fabricating patterned MIS system, viz. a pre–patterned conductive electrode on which the catalytic electrodes are electrodeposited is required.

Amorphous Si (a–Si) is a photoconductive material with a short ambipolar diffusion length of about 115 nm [36–39]. It is a renowned light absorber with a direct bandgap of 1.7 eV, significantly overlapping with the solar spectrum [40–42]. Owing to the photoconductive nature of a–Si, electrochemical reduction could selectively occur when illuminated [43–46]. Herein, we demonstrate light–guided,

spatially selective, and direct electrodeposition of NiMo, non-noble electrocatalyst for HER [5,18,19], on the a-Si substrate. The desired pattern is constructed as a bitmap image file by computer, and light with the same pattern is illuminated onto the a-Si to induce a virtual electrode by local, photogenerated electrons. Electrochemical reduction by potential pulses generates a correspondingly patterned MIS junction. Interestingly, the MIS junction based on a-Si in this work shows abnormally long lateral electron transport, reminiscent of what was previously observed at the photocathodes based on c-Si [6,7]. This effectively relieves not only the interruption of light transmission, but also the dependence of HER on the distance between neighboring non-noble catalysts.

2.2 Experimental

2.2.1. Materials and reagents

Hydrofluoric acid, sodium hexachloroplatinate(Ⅳ) hexahydrate, sodium tetrachloroaurate(Ⅲ) dihydrate, sodium sulfate, nickel(Ⅱ) sulfamate tetrahydrate, boric acid, sodium molybdate, Ga-In eutectic, potassium hydrogen phthalate, potassium sulfate and potassium hydroxide were purchased from Aldrich. Sulfuric acid, ammonium hydroxide, hydrogen peroxide and hydrochloric acid were obtained from Daejung Chemicals. Highly doped n-type Si(100) wafers (0.001~0.003 Ωcm) were purchased from LG Siltron. To prepare all the solutions, deionized water was used (resistivity of 18.2 MΩ cm).

2.2.2. Preparation of a-Si photocathodes

Highly doped n-type Si(100) wafers were cleaned using a standard Radio Corporation of American (RCA) cleaning procedure [47] and then transferred to a plasma-enhanced chemical vapor deposition (PECVD) chamber for a-Si deposition. Triple layers of p-type a-Si:H (20 nm), intrinsic a-Si:H (500 nm), and n-type a-Si:H (100 nm) were deposited sequentially. The a-Si deposited wafers were diced into 1 cm × 1 cm. The native oxides on a-Si were

removed by the immersion of the electrodes in 1% HF solutions and then transferred to piranha solutions (1:3 H_2O_2:H_2SO_4) for 60 s to grow the chemical oxide. The electrodes were rinsed with deionized water and dried using a N_2 gun. These electrodes were stored in a vacuum desiccator in the dark before use.

2.2.3. Light-guided electrodeposition

Spatially selective electrodeposition was conducted using two different light sources. To demonstrate the idea, we used a laser (632.8 nm He/Ne laser, LASOS Lasertechnik GmbH) as part of a home-built micro-Raman system (Dongwoo Optron Co., Ltd). The laser intensity was 1 mW. For the generation of optical pattern images, a homemade DMD display module (Uninanotech) equipped with a 625 nm LED (Mightex, PLS-0625-030-S) was installed on the BX43 Olympus upright microscope. Under focused light illumination, potential pulses were generated using a CHI 440 electrochemical workstation. All electrochemical experiments were carried out using a standard three-electrode configuration in a homemade Teflon cell. For wiring the working electrode to the a-Si photocathode, the Si backside was scratched, and oxide was removed using a few drops of 1% HF solution only on the scratched area of the Si backside. After rinsing with deionized water, the electrodes

were dried by blowing N_2 (99.9%) gas, and wired with Al conductive tape smeared with a Ga-In eutectic system. Pt wire and Ag/AgCl (3 M NaCl, Bioanalytical System, Inc.) were employed as counter and reference electrodes, respectively. The electrodeposition bath was purged with high purity N_2 gas (99.9%) before applying reduction potentials. Na_2PtCl_6 (1 mM) and $NaAuCl_4$ (1 mM) containing 0.5 M Na_2SO_4 (adjusted to pH 3 with 0.5 M H_2SO_4) as a supporting electrolyte were used for the light-guided spatially selective electrodeposition of Pt and Au, respectively. The NiMo electrodeposition bath contained 130 mM $Ni(SO_3NH_2)$, 50 mM H_3BO_3, and 2 mM $NaMoO_4$ (the pH was adjusted to 4.0).

2.2.4. PEC measurements

A 150 W Xenon arc lamp equipped with a 1.5 G filter was used as the solar-simulating light source. The light intensity was calibrated to 100 mW cm^{-2} using a radiometer (Solar light, PMA-2100) and a pyranometer (PMA-2144). For all electrochemical measurements, the reference electrode and the counter electrode were Ag/AgCl (3 M NaCl, Bioanalytical System, Inc.) and Pt wire, respectively. The potentials versus Ag/AgCl reference electrode (0.209 V vs. NHE) were converted to RHE potential using $E(H^+/H_2)$ = −0.47 V vs. Ag/AgCl, measured using a commercialized RHE electrode

(ALS Co., Ltd). Considering a pH value of 4.5, a potential of −0.47 V was almost consistent with the value predicted by the Nernst equation. Linear sweep voltammetry (LSV) was performed using a CHI 440 electrochemical workstation in deaerated 0.2 M potassium hydrogen phthalate solution with 0.2 M K_2SO_4 as a supporting electrolyte (adjusted to pH 4.5 using 2 M KOH) at a scan rate of 10 mV s^{-1}. The electrolyte was continuously bubbled with N_2 gas. The RHE potential was invariant before and after the LSV measurements, determined by measuring open circuit potential (OCP) versus Ag/AgCl electrode. While recording the LSVs, the solution was circulated at a rate of 5 mL s^{-1} using a peristaltic pump. Before the LSV experiments, cyclic voltammetry (CV) was conducted until the voltammograms were stabilized between +0.4 V and −0.5 V (vs. Ag/AgCl). The influence of oxygen gas evolved at the Pt counter electrode in the long-term stability test at 0 V (vs. RHE) was prevented by the immersion of the Pt counter electrode in a separate chamber connected with glass frits, while the reference electrode was immersed in the main chamber. In addition, the oxygen in the electrolyte was purged with the high-purity H_2 gas (99.9%) to maintain a constant RHE potential. The potential shift was negligible after 25 hours of photoelectrolysis (±5 mV, OCP measured by RHE vs. Ag/AgCl). Capacitance-voltage (C-V) measurements were

conducted using a Gamry Reference 600 (Gamry Instruments, Warminster, PA) with 100 Hz AC frequency under AM 1.5 illumination and dark conditions. Incident-photon-to-current efficiency (IPCE) was obtained using a 150 W Xenon arc lamp combined with a monochromator. The light intensity of the monochromatic wavelength was measured using a radiometer and a pyranometer. Faradaic efficiency was given by: $2n_{H2}F/Q$, where n_{H2} is the total amount of produced hydrogen (mol) analyzed by gas chromatography (YL6100GC, Young Lin Instrument) with our sealed home-built quartz photoelectrochemical cell under a N_2 gas environment. F is the Faraday constant and Q is the total amount of charge (C) passed. It was obtained by integrating the current that flew at 0 V (vs. RHE) for 1 hour.

2.2.5. Calculation of ABPE

For evaluating applied-bias photon-to-current efficiency (ABPE), linear sweep voltammograms were recorded in deaerated pH 4.5 buffer solutions at 100 mV s^{-1} under AM 1.5 illumination. Typical equations for calculating ABPE are given by the following [6,7]:

$$BPE \quad \left[\frac{J(mA\,cm^{-2})\left| \times (1.23 - V_b \right|)(V)}{I(mW\,cm^{-2})} \right] \times 100$$

where J is the photocurrent density, V_b is the potential

versus ideal counter electrode, and I is the incident illumination intensity (100 mW cm^{-2} in this work). We present the ideal ABPE here, which assumes an ideal counter electrode for maximum power point (MPP). The equation for ABPE (ideal) is given by [6,7]:

$$BPE\ \ Ideal\,counter\,electrode) = \ J_{PP} \times V_{MPP}|$$

where J_{MPP} and V_{MPP} are the photocurrent density and potential at the MPP, respectively. The best ABPE, 1.06%, (at D/S = 130/130 μm) is presented here as an example.

2.2.6. Calculation of IPCE

For calculating IPCE, steady-state photocurrent density was measured at 0 V (vs. RHE) under monochromatic illumination generated by a Xe arc lamp and monochromator. The IPCE in this study was determined referring to the formula shown below [6,7]:

$$IPCE = \frac{1239.8\,(V nm) \times \ J(mA\,cm^{-2})|}{P_{ono}\,(mW cm^{-2}) \times \lambda\,(nm)}$$

where P_{mono} is the monochromated illumination power density and λ denotes the wavelength.

2.3 Results and Discussion

2.3.1. Demonstration of light-guided electrodeposition

In this system, a-Si was deposited on highly doped n-type Si(100) by plasma-enhanced chemical vapour deposition. To overcome the inherent low photo-induced voltage, we prepared a-Si with a buried p-i-n junction for high open circuit voltage [5]. A protective layer on the Si-based photoelectrode, on which electrodeposition is to occur, is essential because of the vulnerability of the Si surface under aqueous electrochemical conditions. For this purpose, we formed chemical oxide, denoted as SiO_x herein, by immersing the a-Si photoelectrodes in mixed solutions of H_2SO_4 and H_2O_2 after complete removal of the native oxide. The chemical oxide is thin enough to transfer photogenerated charge carriers by tunneling and also serves as an insulating layer to prevent direct contact of the electrolyte solution with the Si-based photoelectrode surface over a wide range of pH values and potentials [48,49]. In addition, the lower defect density of the chemical oxide than the native oxide, i.e., fewer recombination sites, contributes to higher PEC activity [48,49].

In order to demonstrate a proof-of-concept of the light-guided electrodeposition technique using the photoconductivity of a-Si, we patterned one of the

representative electrocatalysts, Pt. As illustrated in Fig. 2-1, a typical three electrode configuration enables the electrochemistry, and a 632.8 nm He/Ne laser is focused on the substrate through the aqueous electrolyte solution that contains Pt precursor ions. Under illumination, an electric potential pulse for Pt electrodeposition is applied via the highly doped Si wafers underneath the a-Si. The applied potential leads to Pt nanoparticles that appear at the illuminated sites (Fig. 2-2). The electrochemically generated Pt nanoparticles are stable and adhesive to the oxide surface, as confirmed by the negligible loss in the optical images taken before and after several washing processes (Fig. 2-3). The HRTEM image in Fig. 2-2 shows the polycrystalline Pt nanoparticles on a-Si. The chemical oxide film formed by the wet chemical process herein was about 1 to 2 nm thick. This result indicates that the electrons produced by focused light on the photoconductive a-Si are used for faradaic reduction which takes place nowhere but the illuminated spot (Fig. 2-4). This is not surprising in that the ambipolar diffusion length in a-Si is less than 115 nm. By making use of this phenomenon, we can enable mask-free light-guided direct electrodeposition on a-Si.

For rapid patterning on larger areas, we replaced the laser illumination module with a red LED (625 nm) combined with a digital micromirror device (DMD) to create the optical

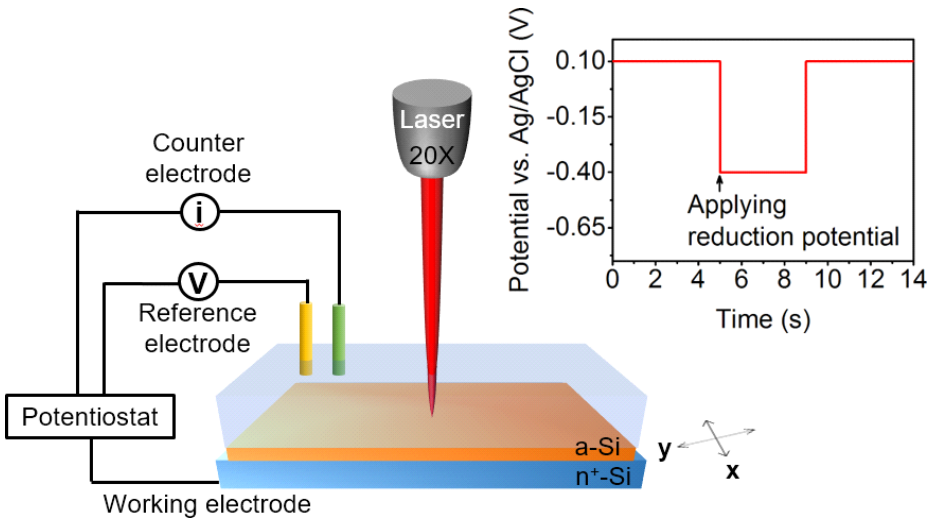

Fig. 2-1 Schematic view of the light-guided electrodeposition experimental setup with 632.8 nm laser illumination.

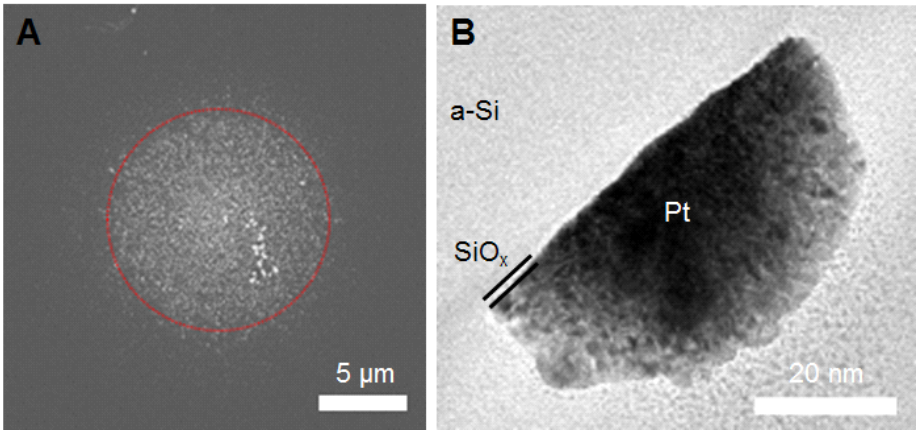

Fig. 2-2 (A) Top view SEM image of electrodeposited Pt nanoparticles (red circle: illuminated area with laser). (B) Cross-sectional HRTEM image of the single Pt nanoparticle/SiO_x/a-Si interface. The thickness of the SiO_x layer was 1 to 2 nm.

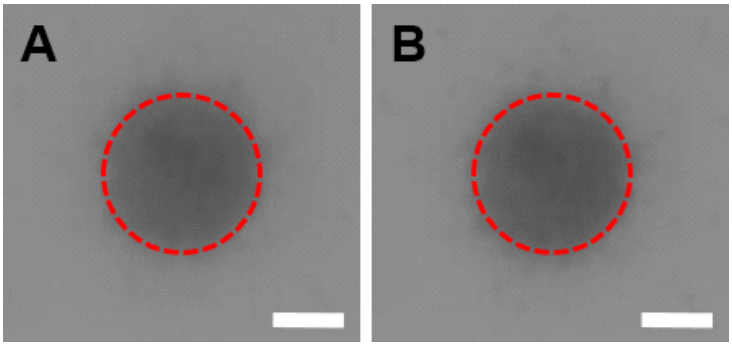

Fig. 2-3 Optical images of electrodeposited dot-shaped Pt pattern captured (A) before and (B) after washing process. Dotted lines in red represent the illuminated area with laser (Scale bar: 5 μm).

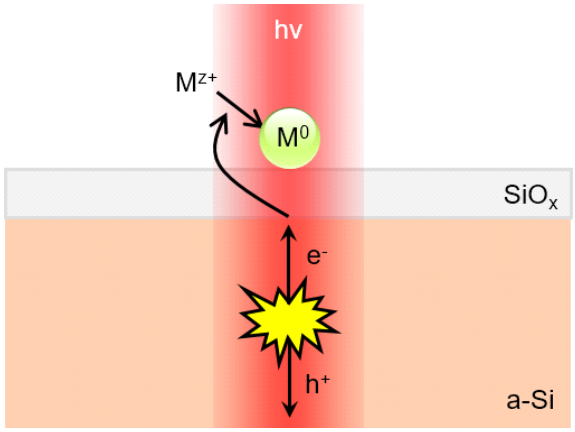

Fig. 2-4 Schematic illustration of the mechanism for light-guided electrodeposition.

image corresponding to that drawn in the computer (Fig. 2-5). As shown in Fig. 2-6A, the resulting light images loaded to the DMD board were focused on the a-Si surface through a 2× objective lens. The maximum size of the light images produced using a DMD was 13 mm × 10 mm and the minimum line width was around 100 mm. Cyclic voltammetry was conducted under the focused LED light with the pattern of a bear face (Fig. 2-6A) onto the a-Si substrate under the same electrolyte conditions as shown in Fig. 2-1. Since the current during the reverse scan was greater than that during the initial forward scan, we can see that the a-Si surface is irreversibly modified with a conductive material that can act as an electrode (Fig. 2-7). Pt in this case is electrodeposited during the initial negative potential scan. Compared with the voltammogram under illumination, almost negligible current and no electrodeposition of Pt were observed under the dark conditions (Fig. 2-7). At a constant potential of −0.4 V (vs. Ag/AgCl) for 180 s, Pt nanoparticles were deposited in the same pattern as the light image created using a DMD (Fig. 2-6B). The current-time curve recorded at −0.4 V (vs. Ag/AgCl) during the Pt electrodeposition is shown in Fig. 2-8.

To look into the role of light in this system, we recorded the total charge passed throughout the electrodeposition as a

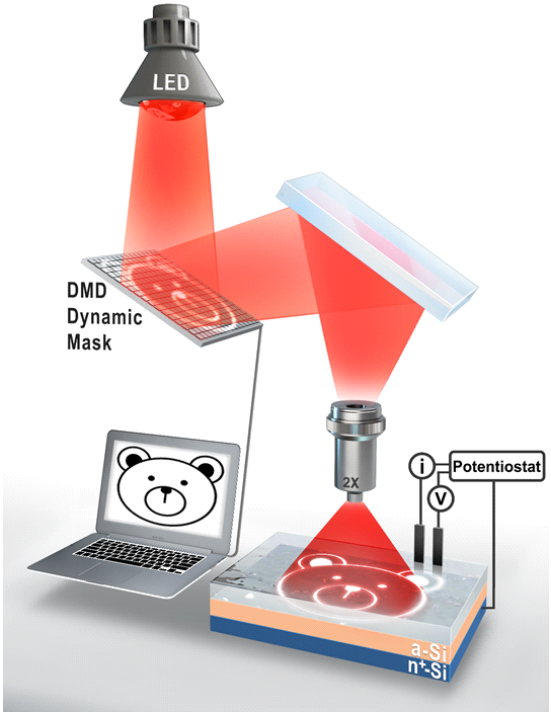

Fig. 2-5 Schematic view of the DMD display system for LED-based electropatterning.

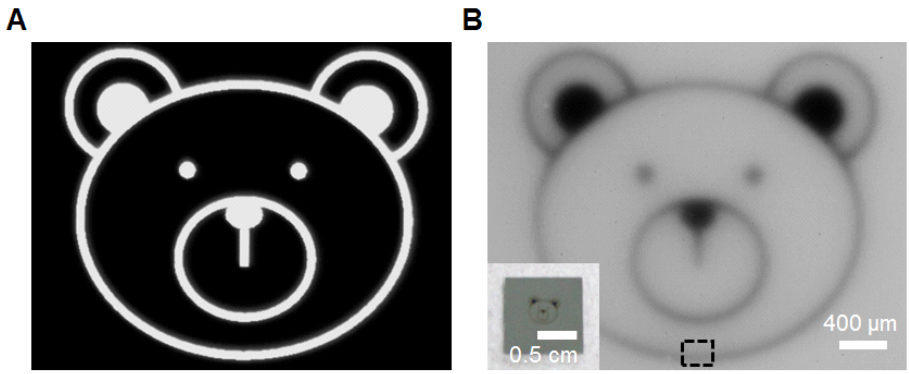

Fig. 2-6 (A) Image of the photomask generated using a 625 nm LED and DMD display. (B) Optical image of the electrodeposited Pt pattern that corresponds to the photomask loaded onto the DMD. The inset shows the photograph of the pattern formed on the a-Si substrate.

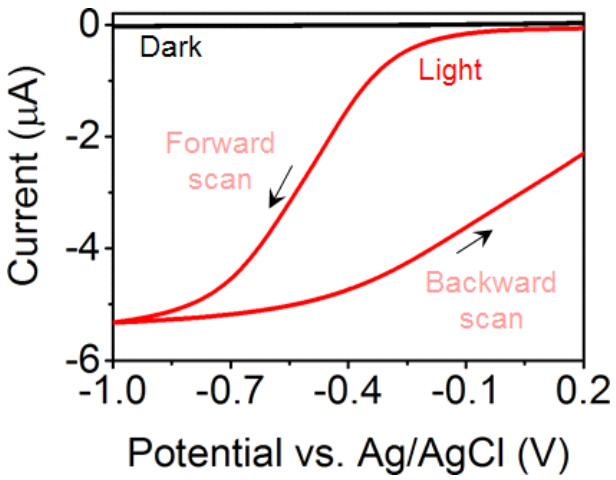

Fig. 2-7 Cyclic voltammogram recorded during Pt electrodeposition under shaped illumination (shown in Fig. 2-6A).

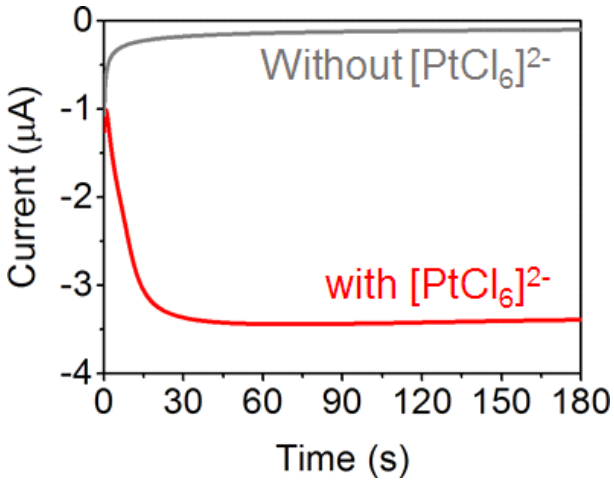

Fig. 2-8 Current-time curve recorded at −0.4 V (vs. Ag/AgCl) for 180 s. Red and gray lines represent the *i*-*t* curve in the presence and absence of Pt precursors in electrolyte solutions, respectively.

function of the diameter of the light images (Fig. 2-9). The total charge passed has a linear relationship with the illuminated areas that coincide with the areas of the actually deposited Pt dots. In addition, the total charge linearly increases with the number of dots generated using a DMD (Fig. 2-10). These results reveal that the light-guided electrodeposition reproducibly produces the pattern that exactly corresponds to the loaded images on the DMD, and the deposition reaction takes place uniformly over the illumination site. The ultimate resolution of this patterning method is about 100 μm when using a 2× objective lens, as shown in Fig. 2-11. As confirmed by Fig. 2-2, the spatial resolution of our patterning method is limited by the size of the illuminated light spot, ~10 micrometer in diameter, made by a laser through a 20× objective lens.

2.3.2. Application of light-guided electrodeposition to the non-noble HER catalyst, NiMo

The proposed patterning method can be applied to the electrodeposition of NiMo, a well-known non-noble catalyst for the hydrogen evolution reaction (HER) on the a-Si substrate. Reduction potential pulses at -0.9 V (vs. Ag/AgCl) were applied for 10 s, followed by open circuit potentials (+0.35 V vs. Ag/AgCl) for 5 s. Precursor ions are

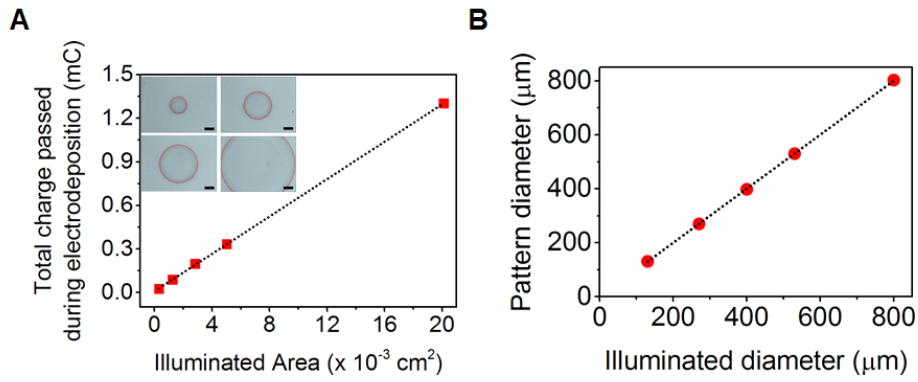

Fig. 2-9 Effects of dynamic light pattern generated by 625 nm LED and DMD display on light-guided electrodeposition of Pt at −0.4 V (vs. Ag/AgCl) for 180 s. (A) Total charge passed during Pt electrodeposition under light with various diameters (Scale bar in inset images: 100 μm). The total charge was calculated by subtracting the integrated area of *i*−*t* curve in the absence of Pt precursors from in the presence of them. (B) Linear correlation between illuminated area and the size of pattern electrodeposited by light on a-Si (slope: 1.00 ± 0.02 and intercept: 0.044 ± 0.026 with an R^2 = 0.999). The diameters of the electrodeposited patterns were measured by the ImageJ program.

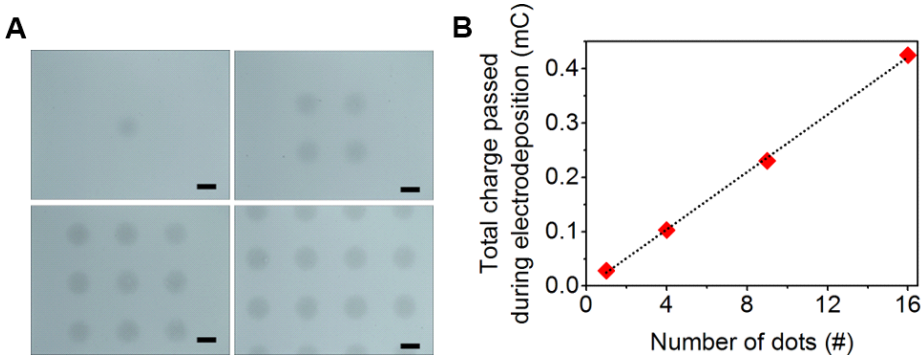

Fig. 2-10 (A) Optical images of Pt spots electrodeposited by light (Scale bar: 400 μm). (B) Linear increase of total charge passed during electrodeposition of Pt with the number of light spots represented by the circle.

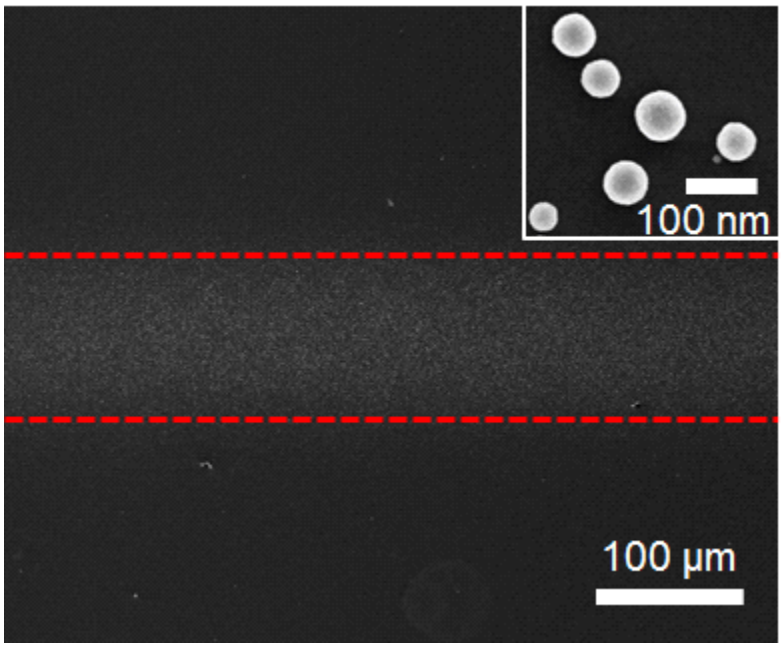

Fig. 2-11 SEM image of the selected area marked in (as dotted rectangle in Fig 2-6B). Pt nanoparticles consisting of a line pattern are shown in the inset image. Dotted lines in red indicate the illuminated area.

replenished during the period of the resting potential so that the potential pulse technique can yield a more dense and uniform NiMo film. As shown in the images taken during the electrodeposition of NiMo (Fig. 2-12), the illuminated sites are blackened by the deposited NiMo as a result of 80 reduction pulses. After the programmed potential bias is applied, a greenish film with a dot shape appears on the a-Si substrate (Fig. 2-13). Consistent with the results of Pt electrodeposition, NiMo patterning reflects the reliability and expandability of the proposed method. Fig. 2-14 shows the scanning electron microscopy (SEM) images of the top and cross-section of the NiMo catalysts on the a-Si. The deposited NiMo is a roughened conformal film containing cracks and pinholes. This morphology originates from the hydrogen bubbles that appear during the deposition process referring to the reported literature [18]. The NiMo films are about 150 nm thick for 80 reduction pulses applied. The Ni/Mo ratio calculated using X-ray fluorescence (XRF) spectroscopy is about 5.7, which is similar to the previously reported results (Fig. 2-15) [18,19].

2.3.3. Long, lateral electron transport in a-Si

As illustrated in the schematic energy band diagram of Fig. 2-16, the p-i-n type of a-Si has a band structure similar to that of the p-type [50], indicating that it can function as a

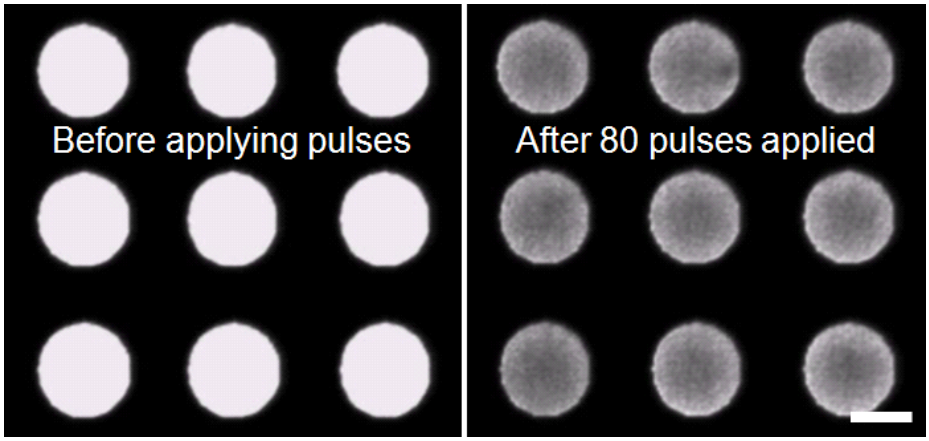

Fig. 2-12 Change in the image during the NiMo electrodeposition under dot-patterned illumination.

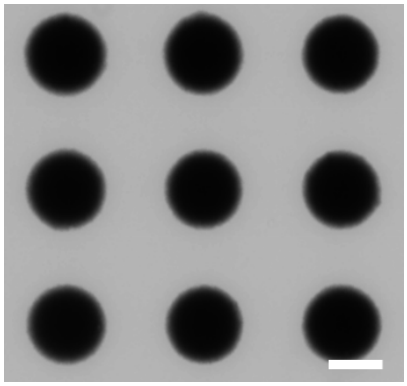

Fig. 2-13 Optical image of the dot-patterned NiMo catalyst electrodeposited from the photomask shown in (Fig. 2-12), generated using a DMD.

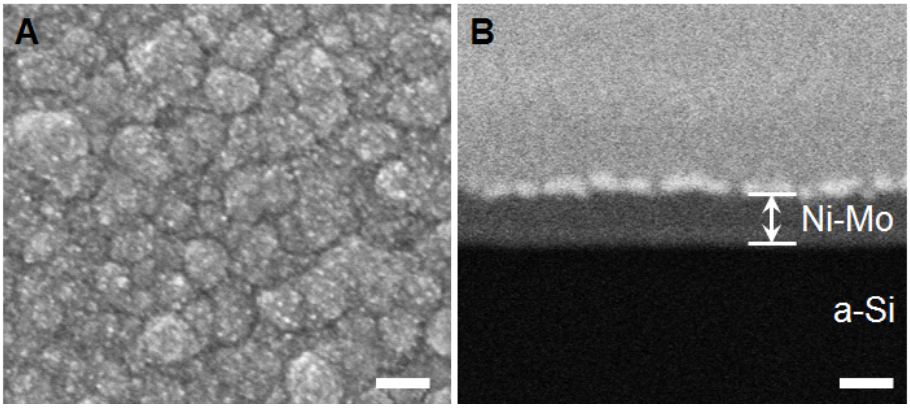

Fig. 2-14 (A) Top view and (B) cross-sectional SEM image of the NiMo film. The cross-sectional image was taken in EsB mode of the SEM device.

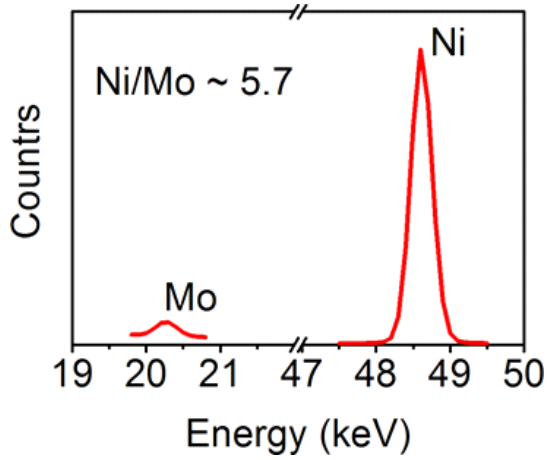

Fig. 2-15 XRF spectra of Ni and Mo for quantitative analysis of the Ni/Mo ratio.

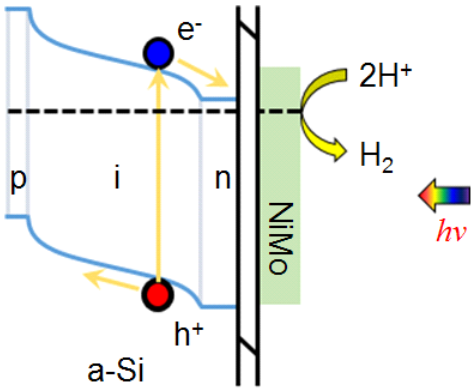

Fig. 2-16 Schematic energy band diagram of the NiMo/SiO_x/a-Si junction for PEC HER.

photo-generated electron supplier for the solar-driven electrochemical reduction of protons. Electrons from excitons created by light absorption migrate to the semiconductor/electrolyte interface following an electric field across the MIS junction, and transfer through SiO_x to the NiMo catalysts where faradaic reduction takes place. In Fig. 2-17A, we see that the current density from the linear sweep voltammetry (LSV) remarkably increases in the presence of NiMo compared with the bare a-Si surface. The influence of the number of patterned NiMo dots on the current for hydrogen evolution has an implication on how PEC HER occurs using photo-induced electro-patterned NiMo. As reported in the previous work performed with the $Pt/Ti/SiO_2/p-Si(100)$ photocathode [7], current densities for all voltammograms should be saturated at sufficiently high overpotential to similar limiting current irrespective of the number of NiMo dots. It is because HER should take place at the bare photoelectrode surface as well as the catalyst illuminated if the spillover-assisted hydrogen evolution governs the photoelectrode system [7]. However, the current density at 0 V vs. reversible hydrogen electrode (RHE) in the proposed system increases in proportion to the number of NiMo dots, indicating the augment of surface coverage by the NiMo catalyst for the constant exposed photoelectrode area. Negligible current was observed without

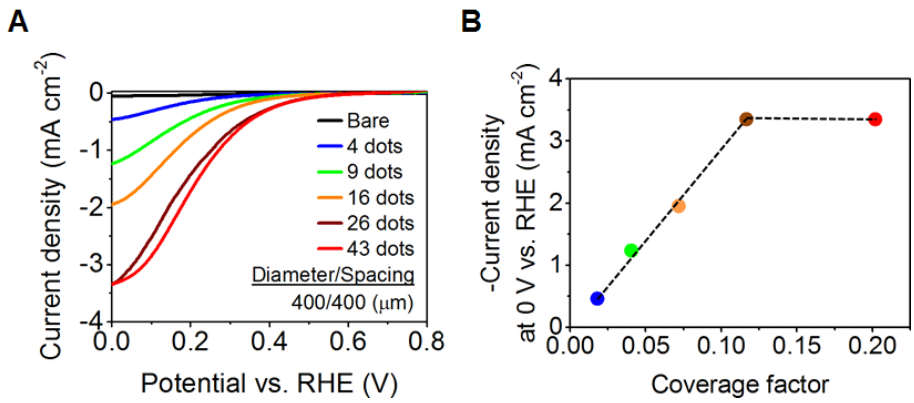

Fig. 2-17 (A) Linear sweep voltammograms for HER at the NiMo pattern/SiO_x/a-Si junction photocathode in deaerated 0.2 M aqueous potassium hydrogen phthalate buffer (pH 4.5) with 0.2 M K_2SO_4 as a function of the number of NiMo dots, in which individual dot areas are constant, 400 μm in diameter, and neighboring dots are equally spaced by 400 μm. So, more dots mean a larger net area of NiMo arrays that are at the center of the electrode. (B) The correlation between the NiMo coverage factor and the current density at 0 V vs. RHE. The colors of circles correspond to those of the curves in (A).

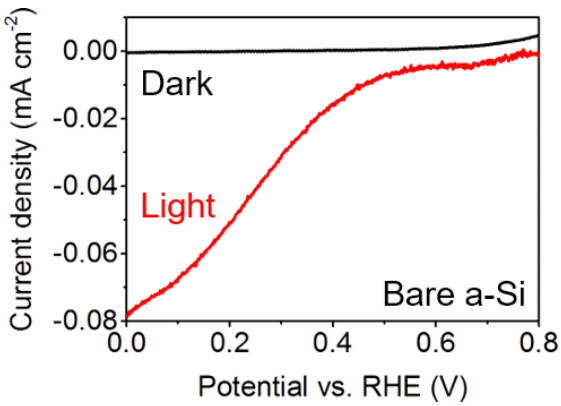

Fig. 2-18 Linear sweep voltammograms for HER at bare a-Si photocathode under light and dark conditions.

illumination (Fig. 2-18). This result corroborates the role of patterned NiMo as a catalyst, which lets photogenerated electrons drain out effectively for light-driven electrochemical HER. As shown in Fig. 2-17B, the current density at 0 V (vs. RHE) is saturated at 60% (about 0.12) of the highest coverage tested (about 0.20) where diameter and spacing are 400 and 400 μm, respectively. Keeping in mind negligible catalytic activity at the bare a-Si surface covered with SiO_x for HER, the photogenerated electrons must travel much longer distances through the a-Si to reach the catalytic sites than in bulk a-Si. This observation indirectly supports the long-lateral electron diffusion along the a-Si edge. Based on these results, Fig. 2-19 illustrates the electron transport through the NiMo pattern/SiO_x/a-Si photocathode for hydrogen generation.

To demonstrate the effects of long-distance lateral electron transport in a-Si and transfer to the semiconductor/electrolyte interface, we conducted experiments of 'remote electrodeposition'. As shown in Fig. 2-20A, a line of Au was electrodeposited in the same way which was apart by 1600 μm from the center of the prepatterned Pt line, which was also exposed to the electrolyte containing Au precursors. As shown in Fig. 2-20B and Fig. 2-21, Au nanoparticles grow on the bare a-Si where it is illuminated, as well as on pre-patterned Pt

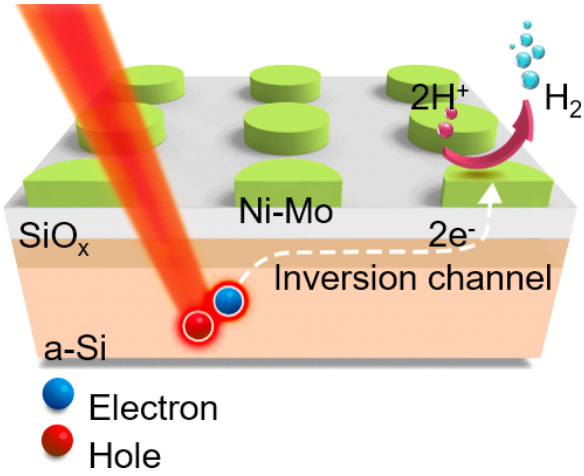

Fig. 2-19 Schematic illustration of the HER operation mechanism at the NiMo pattern/SiO_x/a-Si photocathode.

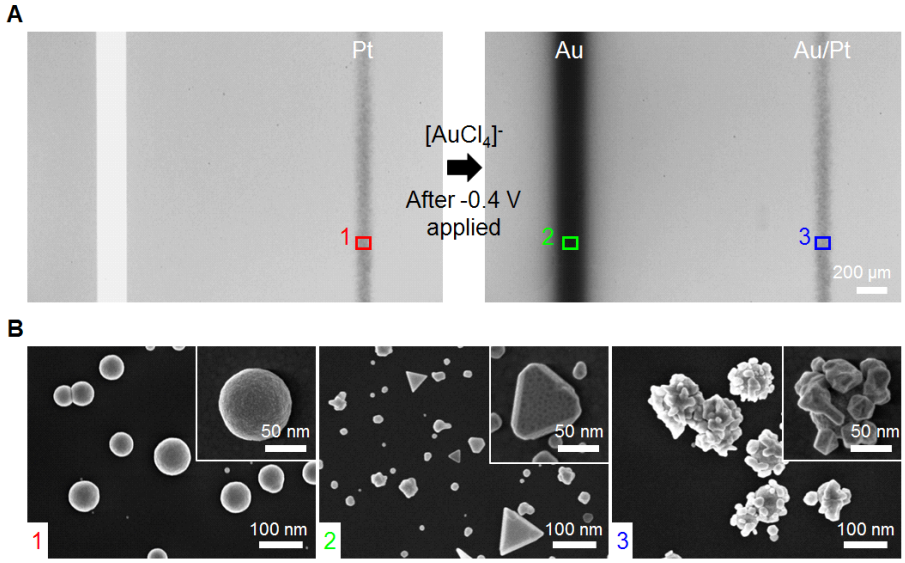

Fig. 2-20 Remote electrodeposition to investigate long-distance lateral electron transport in a-Si. (A) Optical images of light-guided Au electro-patterning 1.6 mm from the pre-patterned Pt line feature. (B) SEM images at each area marked on panel A.

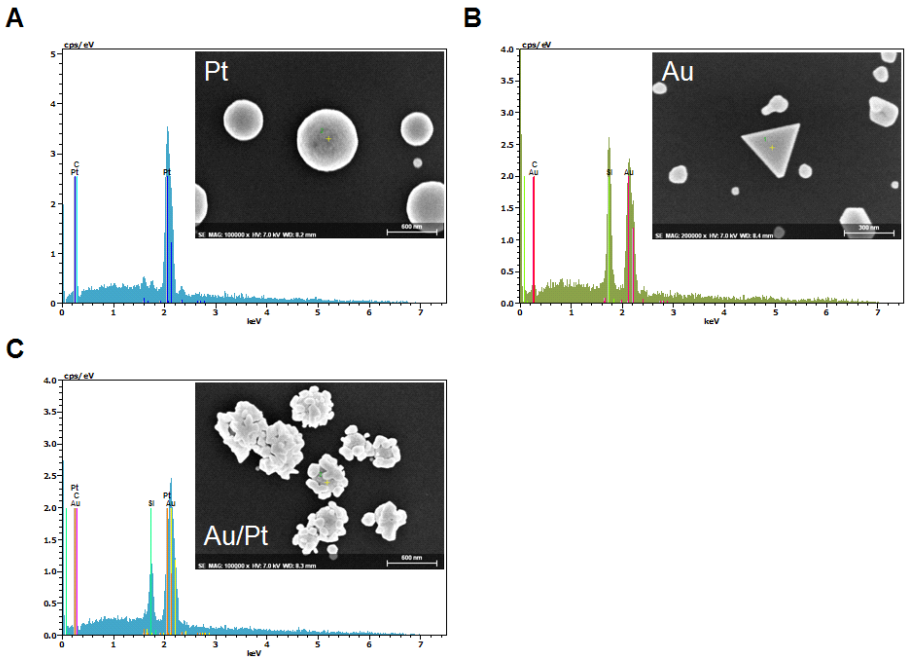

Fig. 2-21 EDS spectra of Pt, Au, and Au/Pt nanoparticles generated by electrodeposition as in Fig. 2-20. The Pt nanoparticles were deposited prior to Au electrodeposition and the Au particles electroplated on the illuminated area. Au/Pt represents the Au nanoparticles electrodeposited on the prepatterned Pt nanoparticles.

nanoparticles where it is dark. The cathodic current for Au deposition is much higher in the presence of the pre-patterned Pt. Interestingly, a little hump is found at about 4 s in the i-t curve of Au electrodeposition with pre-patterned Pt, while it does not appear on the bare a-Si surface without Pt (Fig. 2-22). The current hump is usually observed due to overlapping diffusion fields in electrochemical systems in which nanoparticles grow [31]. The Au nanoparticle was electrodeposited nowhere else under dark conditions. Referring to the study on the metal/self-assembled monolayer/metal system [51-53], we can assume that once a metal seed is formed on SiO_x/a-Si by tunneling, charge transfer to it would become more facile. Higher density of states due to the presence of the metal seed reportedly contributes to more probable electron transfer through the thin insulating layer [51-53]. As illustrated in Fig. 2-23, faradaic reduction can occur at the metal structures as well as in the illuminated region of a-Si, indicating the long-distance transport through the a-Si. Because of this phenomenon, single-shot patterning on a large area of a-Si using the LED-DMD combination is preferred for continuously writing with a focused laser beam. The electrochemical growth continues where it was previously scanned but is currently in the dark so that the electrodeposited lines are hardly controlled (Fig. 2-24).

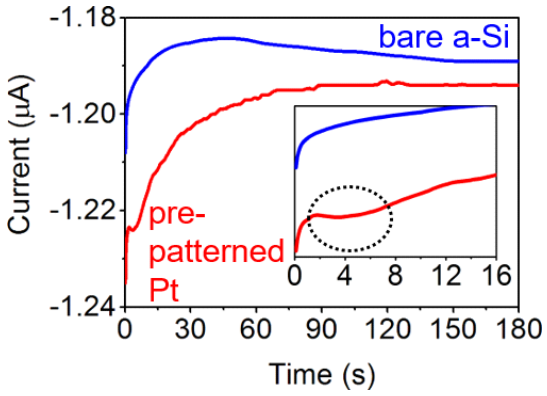

Fig. 2-22 Current-ime (i-t) curves recorded during the Au electrodeposition in the absence and the presence of pre-patterned Pt. The inset shows a little hump (marked by the black dotted circle) at the initial stage.

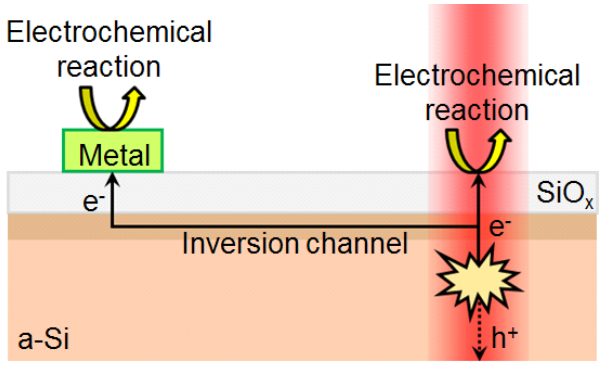

Fig. 2-23 Schematic illustration of long-distance lateral electron transport along the inversion layer in a-Si.

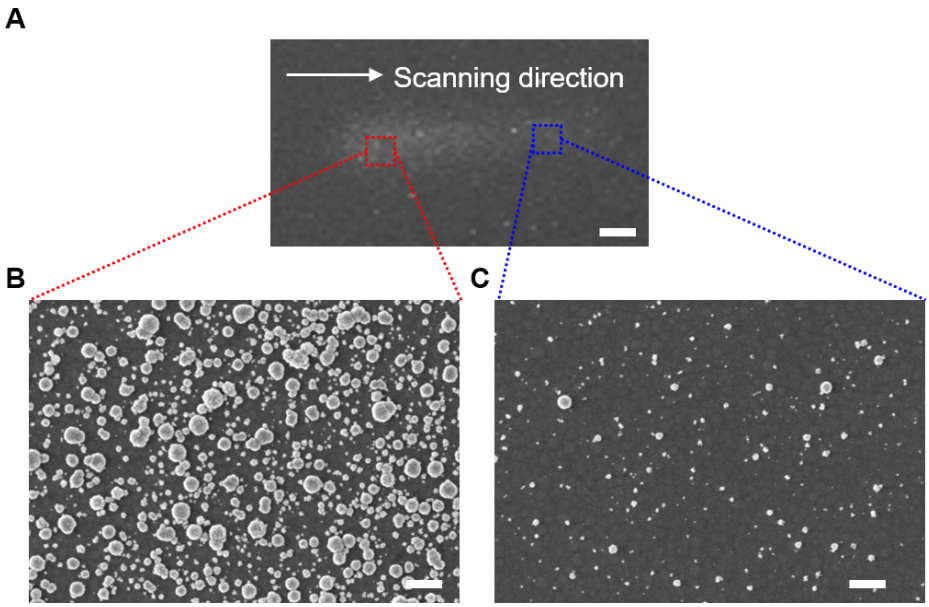

Fig. 2-24 (A) SEM images of light-induced electrodeposited Pt line pattern obtained by scanning substrate under bias at −0.4 V (vs. Ag/AgCl). Substrates were moved at a rate of 1 μm s^{-1}. (B) and (C) show the area where the scanning starts and ends, respectively (scale bar in A: 5 μm, B and C: 200 nm).

To further examine the dependence of PEC HER activity on lateral electron transport, we measured the local photocurrents as the focused 530 nm LED light was displaced from the pre-patterned NiMo (Fig. 2-25). The photocurrent decreases by increasing the distance from the NiMo catalyst, presumably attributed to electron-phonon scattering and electron-hole recombination. However, as previously observed in the remote electrodeposition experiments, the photocurrent can flow even when the light source is illuminated at much longer (1 mm) distance than the ambipolar diffusion length of a-Si (115 nm) from the metallic collector, NiMo. This long-distance travel of electrons in a-Si may be unfavorable for the operation mechanism of spatially selective electrodeposition induced by local illumination. However, the patterning resolution is not seriously dependent on lateral electron transport because electron transfer to the electrolyte solutions in the dark region occurs not through the bare a-Si surface, but through the MIS junction only, as shown in Fig. 2-17 and 2-23. Esposito *et al.* and Ji *et al.* [6,7] suggested that diffusion along unexpectedly long distance in c-Si is ascribed to the inversion layer beneath the oxide layer. The proposed NiMo/SiO_x/a-Si photoelectrode for HER also exhibits the light-induced transition in the capacitance-voltage curve at +0.35 V (vs. RHE), which is similar to the behavior

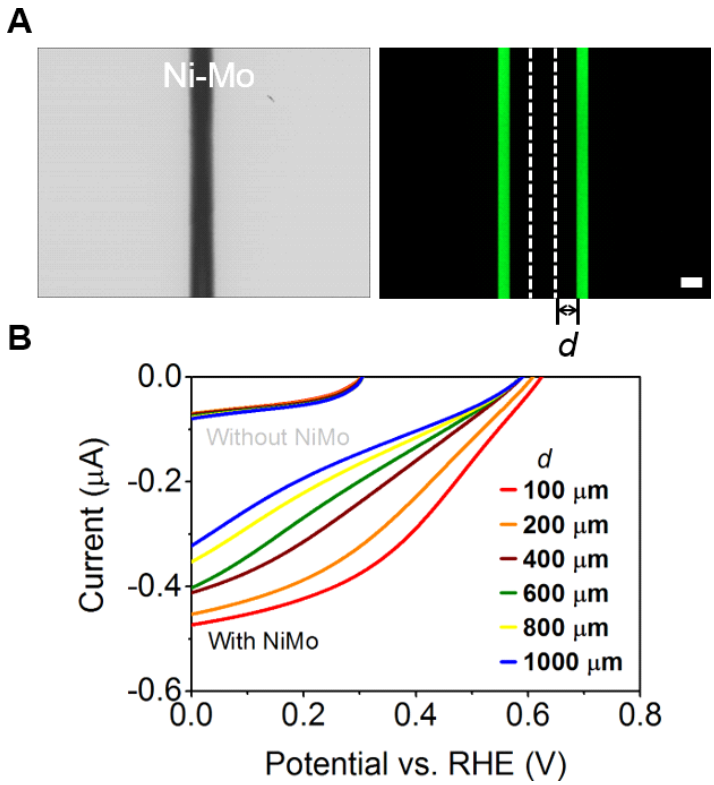

Fig. 2-25 Local photocurrent in deaerated pH 4.5 buffer due to NiMo pattern. (A) Left: optical image of a line of electrodeposited NiMo. Right: scheme of local photocurrent measurement under 530 nm LED illumination generated by DMD (scale bar: 100 μm). (B) LSVs to probe local PEC activity as a function of illumination distance from the NiMo, which acts as an electron collector. LSVs under the same conditions without the NiMo pattern are presented for comparison.

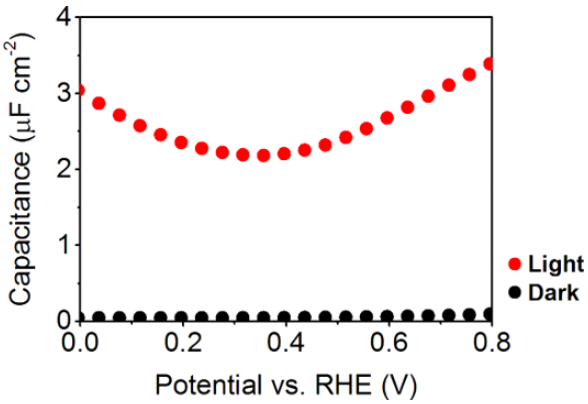

Fig. 2-26 Capacitance-voltage curves recorded for a SiO_x/a-Si photocathode under simulated AM 1.5 illumination and dark conditions measured at 100 Hz AC frequency.

observed for c-Si (Fig. 2-26) [7]. In line with the previous reports on c-Si, we postulate that protons at a negative bias may play a critical role in electron transport at silicon/electrolyte interfaces because protons can diffuse in the thin oxide layer by virtue of intimate chemical attraction with the Si surface and the oxide layer [7,54-56].

2.3.4. Effect of patterned NiMo on a-Si photocathode on PEC HER

Despite the lateral transport of photo-generated electrons through the inversion channel, the long distance does not favor current density due to electron-phonon scattering and recombination. On the other hand, too short channel length between the patterned catalysts suffers from light transmission to the underlying a-Si, which results in the decrease of current density (Fig. 2-27). Thus, it is important to compromise both factors and find the proper spacing among the NiMo patterns. Prior to the systematic investigation of the spacing effect, we determined the optimal amount of catalyst electrodeposited for each spacing by comparing the current density at 0 V (vs. RHE). Narrower spacing requires fewer pulses for NiMo electrodeposition (Fig. 2-28 and 2-29). As the spacing among the catalysts gets narrower, a less amount of NiMo catalyst for individual dots is needed to reach the maximal current (Fig. 2-30).

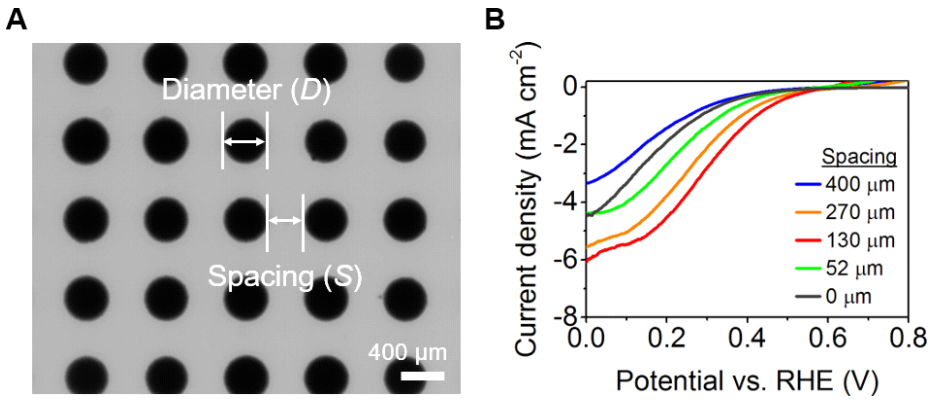

Fig. 2-27 (A) Optical image of the NiMo pattern/SiO_x/a-Si photocathode. (B) Linear sweep voltammograms for various spacings of NiMo dots of constant diameter, 400 μm. A spacing of 0 μm indicates the photocathode of non-patterned NiMo/SiO_x/a-Si.

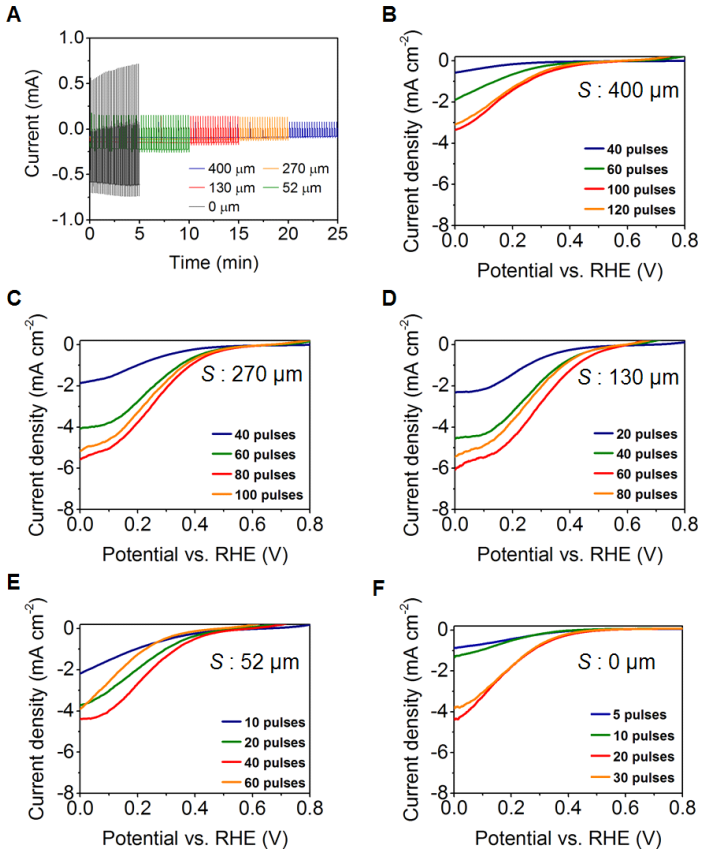

Fig. 2-28 Optimization of amount of NiMo catalyst for each spacing value on a-Si photocathode. (A) Current-time ($i-t$) curves for optimized light-guided electrodeposition of NiMo with various spacing. The results of LSV for different amounts of NiMo loaded, which were controlled by the number of reduction pulses. The spacing was varied at (B) 400, (C) 270, (D) 130, (E) 52, and (F) 0 μm under simulated AM 1.5 illumination. The diameter of all NiMo dots was constant, 400 μm.

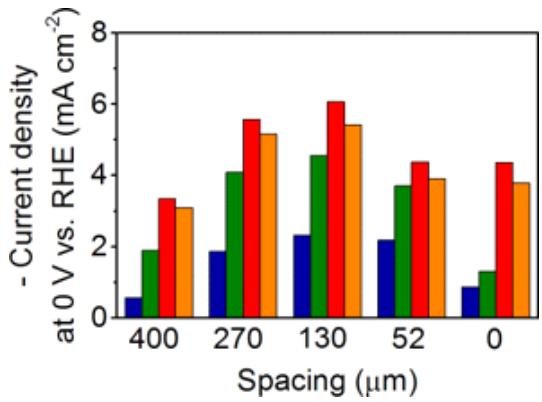

Fig. 2-29 Histograms of the photocurrent at 0 V (vs. RHE) with various amounts of NiMo loading at each of the different spacings (Histogram colors correspond to the number of the potential pulses presented in panel B-E of Fig. 2-28).

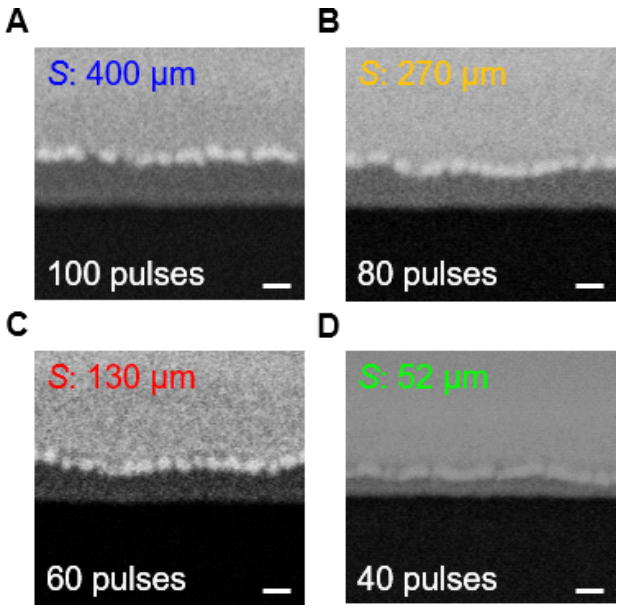

Fig. 2-30 Cross-sectional SEM images of NiMo films with different optimal amounts for different spacings. The optimized thicknesses were roughly (A) 150 nm, (B) 100 nm, (C) 80 nm, and (D) 50 nm (scale bar is 100 nm).

From the linear sweep voltammograms in Fig. 2-27B, the best spacing for 400 μm diameter NiMo dots was determined to be 130 μm for the hydrogen evolution. Spacing wider than 130 μm leads to lower current density. This can be understood by taking into account the limited lateral electron transport along the inversion layer, which is deterred by electron-phonon scattering and recombination. On the other hand, the current density also drops for spacings shorter than 130 μm, presumably because of the significant optical loss caused by absorption and/or scattering by the NiMo catalysts. This is confirmed by the total reflectance (TR) from NiMo pattern/SiO_x/a-Si in the wavelength ranging from 300 to 800 nm as a function of spacing among the NiMo dots (Fig. 2-31). TR keeps on decreasing as the catalysts get closer until the spacing is as short as 130 μm. For more closely patterned NiMo dots including fully covered with NiMo, TR spectra depend on the wavelength. As the spacing is shortened further to be 52 and 0 μm, TR increases at shorter wavelength than 600 nm, probably due to reflection by NiMo, while it continues to decrease in the longer wavelength region. Therefore, TR lets us estimate the coverage of the NiMo catalyst on SiO_x/a-Si for maximal light absorption. In addition, we confirm the same trend of spacing effects on PEC HER at the NiMo dots of 130 μm in diameter (Fig. 2-32).

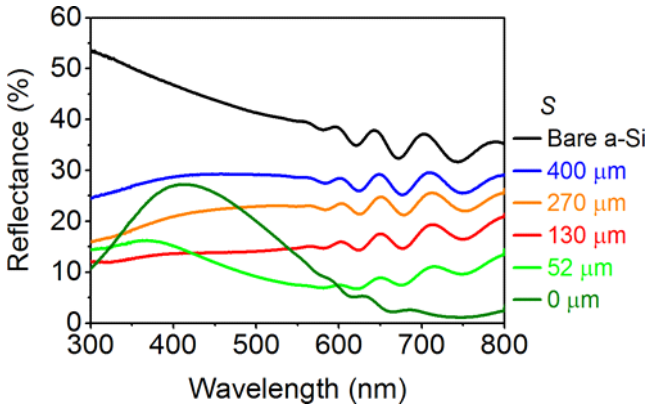

Fig. 2-31 Variation in the total spectral reflectance of NiMo pattern/SiO_x/a-Si with spacing, in which the diameter of NiMo catalyst was constant, 400 μm. Here 0 μm refers to the a-Si substrate whose surface was fully covered with NiMo catalyst.

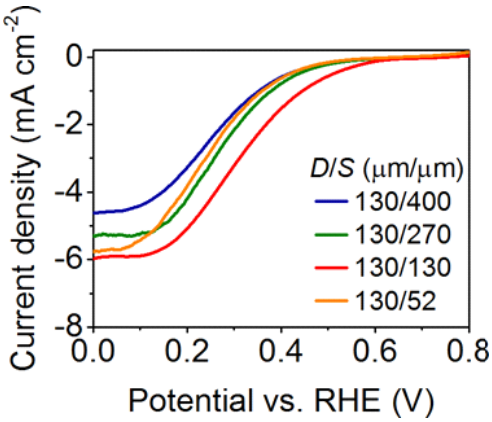

Fig. 2-32 Linear sweep voltammograms for various spacing of NiMo dots under constant pattern diameter, 130 μm.

Varying the diameter of the uniformly spaced NiMo dots provides further information on the effect of the catalyst pattern on the PEC activity. The linear sweep voltammograms in Fig. 2-33 indicate that the onset potentials (at J = -0.1 mA cm^{-2}) and V_{MPP} (MPP, maximum power point) shift positively as the dot becomes smaller, resulting in higher ABPE (calculated assuming an ideal counter electrode, Fig. 2-34). The current density at 0 V (vs. RHE) continues to increase as the diameter decreases from 1200 to 800 μm, and reaches a plateau at less than 800 μm. The best ABPE in the proposed system is 1.06% for a diameter/spacing (D/S) of 130/130 μm (Fig. 2-35). The principle that underlies this phenomenon is unclear yet. One of the reasons may be that the edge of the catalyst is located near the bare photoelectrode surface [7,57]. Further research to collect direct evidence is underway. The current density of -6 mA cm^{-2} (at 0 V vs. RHE) and the V_{OC} of 620 mV are close to the inherent performance in Pt/planar a-Si photocathodes [50], indicating the sufficient non-noble catalyst loading with the negligible optical losses by the catalysts. The ABPE of this system, which is lower than that of photocathodes based on c-Si, results from the low incident photon-to-current conversion efficiency (IPCE) at short wavelengths and in the near band edge region (Fig. 2-36). Such behavior was previously reported in the

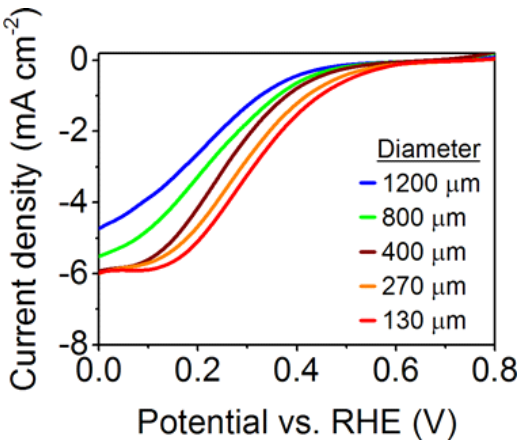

Fig. 2-33 Linear sweep voltammograms for a variety of catalyst diameters with a constant spacing of 130 μm.

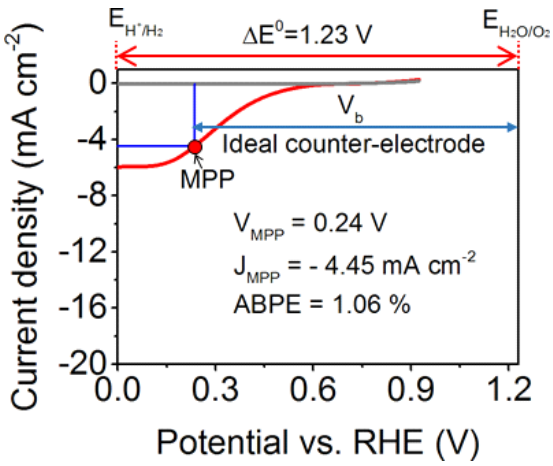

Fig. 2-34 Calculation of ABPE.

		D/S, μm/μm	Coverage factor, $\pi D^2/4(S+D)^2$	J (at V=0 vs. RHE), mA cm^{-2}	V_{OC} (at J = -0.1 mA cm^{-2}), V vs. RHE	V_{MPP}, V vs. RHE	J_{MPP}, mA cm^{-2}	ABPE, %
S variation	D: 400 μm	400/400	0.20	-3.34	0.49	0.17	-1.72	0.29
		400/270	0.28	-5.56	0.57	0.21	-3.57	0.76
		400/130	0.45	-5.98	0.57	0.22	-4.08	0.94
		400/52	0.61	-4.38	0.52	0.17	-2.88	0.54
	D: 130 μm	130/400	0.047	-4.62	0.55	0.20	-3.20	0.64
		130/270	0.083	-5.29	0.56	0.20	-4.17	0.84
		130/130	0.20	-5.98	0.62	0.24	-4.45	1.06
		130/52	0.40	-5.76	0.53	0.19	-4.06	0.77
D variation		1200/130	0.64	-4.73	0.53	0.19	-2.71	0.52
		800/130	0.58	-5.52	0.55	0.20	-3.33	0.65
		400/130	0.45	-5.98	0.57	0.22	-4.08	0.94
		270/130	0.36	-5.99	0.61	0.23	-4.22	0.95
		130/130	0.20	-6.00	0.62	0.24	-4.45	1.06

Fig. 2-35 HER performance for various D/S values at NiMo pattern/SiO_x/a-Si photocathodes from LSV. MPP denotes maximum power point.

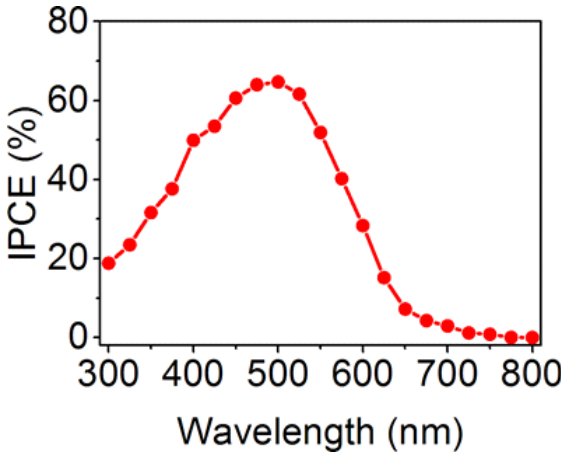

Fig. 2-36 IPCE measured using monochromatic light from a Xenon arc lamp and an applied bias of 0 V (vs. RHE). IPCE measurements were conducted at *D*/*S* of the 130/130 μm NiMo pattern/SiO_x/a-Si photocathode.

external quantum efficiency (EQE) of a-Si solar cells [58]. The low IPCE at wavelengths shorter than 400 nm is attributed to the recombination at defect sites caused by the B-doped region of p-type a-Si. Fig. 2-37 shows that the proposed system does not suffer from degradation for approximately one day at 0 V (vs. RHE) and the Faradaic efficiency at 0 V (vs. RHE) was 98.4% after 60 minutes of reaction under simulated AM 1.5 illumination.

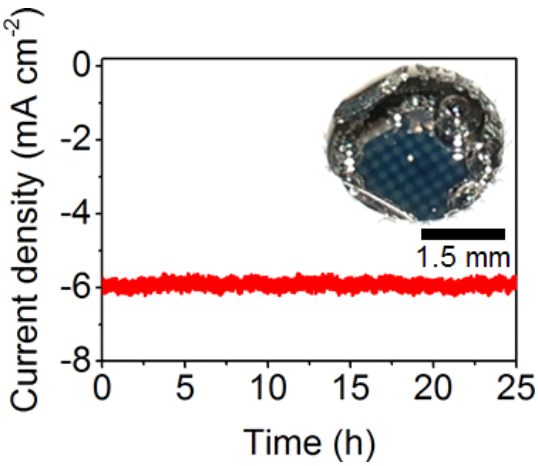

Fig. 2-37 Stability test by chronoamperometry at a constant 0 V (vs. RHE) for 25 h. Durability measurements were conducted at *D*/*S* of the 130/130 μm of NiMo pattern/SiO_x/a-Si photocathode.

2.4 Conclusion

In this study, we have demonstrated a solar-driven photocathode for the water-splitting device fabricated by light-guided NiMo electrodeposition. The computer-aided virtual photomask using a DMD enables direct patterning based on photo-induced electrodeposition on a-Si for flexibility, scalability, and high throughput with high yield compared to typical photolithography. By virtue of this new method, NiMo, which is a well-known nonprecious electrocatalyst for hydrogen evolution, was directly patterned onto the a-Si photoelectrode. The direct patterning of non-noble electrocatalysts for the PEC HER in this work has great potential for further improvement. The patterned MIS junction composed of low cost materials can enhance the PEC activity for HER by integrating additional light trapping structures, high-quality protective layers that have proper band alignment with respect to the hydrogen evolution potentials for reduced electron extinction [3,6,59], optimization of inversion channels to deploy protons, and finer tuning of pattern design and microstructures of catalysts. We expect that the current work will lead to important advances toward efficient, self-biasing, and integrated PEC water splitting for practical commercialization. In addition, this technique has great potential for a wide

range of applications requiring patterned substrates such as biosensors, electronic devices, and the photoelectrode systems related to the energy conversion reaction, e.g. CO_2 reduction and oxygen evolution reaction.

2.5 References

[1] A. Fujishima and K. Honda, *Nature*, 1972, *238*, 37.

[2] Y. W. Chen, J. D. Prange, S. Duehnen, Y. Park, M. Gunji, C. E. D. Chidsey and P. C. McIntyre, *Nat. Mater.*, 2011, *10*, 539.

[3] S. Hu, M. R. Shaner, J. A. Beardslee, M. Lichterman, B. S. Brunschwig and N. S. Lewis, *Science*, 2014, *344*, 1005.

[4] J. Yang, K. Walczak, E. Anzenberg, F. M. Toma, G. Yuan, J. Beeman, A. Schwartzberg, Y. Lin, M. Hettick, A. Javey, J. W. Ager, J. Yano, H. Frei and I. D. Sharp, *J. Am. Chem. Soc.*, 2014, *136*, 6191.

[5] Y. Lin, C. Battaglia, M. Boccard, M. Hettick, Z. Yu, C. Ballif, J. W. Ager and A. Javey, *Nano Lett.*, 2013, *13*, 5615.

[6] L. Ji, M. D. McDaniel, S. Wang, A. B. Posadas, X. Li, H. Huang, J. C. Lee, A. A. Demkov, A. J. Bard, J. G. Ekerdt and E. T. Yu, *Nat. Nanotechnol.*, 2015, *10*, 84.

[7] D. V. Esposito, I. Levin, T. P. Moffat and A. A. Talin, *Nat. Mater.*, 2013, *12*, 562.

[8] J. R. McKone, N. S. Lewis and H. B. Gray, *Chem. Mater.*, 2014, *26*, 407.

[9] T. J. Jacobsson, V. Fjallstrom, M. Edoff and T. Edvinsson, *Energy Environ. Sci.*, 2014, *7*, 2056.

[10] Z. Chen, S. Ye, A. R. Wilson, Y.-C. Ha and B. J. Wiley,

Energy Environ. Sci., 2014, *7*, 1461.

[11] W. D. Chemelewski, H.-C. Lee, J.-F. Lin, A. J. Bard and C. B. Mullins, *J. Am. Chem. Soc.*, 2014, *136*, 2843.

[12] J. J. H. Pijpers, M. T. Winkler, Y. Surendranath, T. Buonassisi and D. G. Nocera, *Proc. Natl. Acad. Sci. U. S. A.*, 2011, *108*, 10056.

[13] M. Aparicio, A. Jitianu and L. C. Klein, *Sol-Gel Processing for Conventional and Alternative Energy*, Springer, New York Heidelberg Dordrecht London, 2012, p. 86.

[14] M. G. Walter, E. L. Warren, J. R. McKone, S. W. Boettcher, Q. Mi, E. A. Santori and N. S. Lewis, *Chem. Rev.*, 2010, *110*, 6446.

[15] A. Heller, D. E. Aspnes, J. D. Porter, T. T. Sheng and R. G. Vadimsky, *J. Phys. Chem.*, 1985, *89*, 4444.

[16] J. Kye, M. Shin, B. Lim, J.-W. Jang, I. Oh and S. Hwang, *ACS Nano*, 2013, *7*, 6017.

[17] P. Dai, J. Xie, M. T. Mayer, X. Yang, J. Zhan and D. Wang, *Angew. Chem., Int. Ed.*, 2013, *52*, 11119.

[18] J. R. McKone, E. L. Warren, M. J. Bierman, S. W. Boettcher, B. S. Brunschwig, N. S. Lewis and H. B. Gray, *Energy Environ. Sci.*, 2011, *4*, 3573.

[19] E. L. Warren, J. R. McKone, H. A. Atwater, H. B. Gray and N. S. Lewis, *Energy Environ. Sci.*, 2012, *5*, 9653.

[20] X. L. Hu, B. M. Cossairt, B. S. Brunschwig, N. S. Lewis

and J. C. Peters, *Chem. Commun.*, 2005, 4723.

[21] M. L. Helm, M. P. Stewart, R. M. Bullock, M. R. DuBois and D. L. DuBois, *Science*, 2011, *333*, 863.

[22] S. C. Marinescu, J. R. Winkler and H. B. Gray, *Proc. Natl. Acad. Sci. U. S. A.*, 2012, *109*, 15127.

[23] M. O' Hagan, M.-H. Ho, J. Y. Yang, A. M. Appel, M. R. DuBois, S. Raugei, W. J. Shaw, D. L. DuBois and R. M. Bullock, *J. Am. Chem. Soc.*, 2012, *134*, 19409.

[24] C. Madden, M. D. Vaughn, I. Diez-Perez, K. A. Brown, P. W. King, D. Gust, A. L. Moore and T. A. Moore, *J. Am. Chem. Soc.*, 2012, *134*, 1577.

[25] H. Kim, J. Kim, H. Yang, J. Suh, T. Kim, B. Han, S. Kim, D. S. Kim, P. V. Pikhitsa and M. Choi, *Nat. Nanotechnol.*, 2006, *1*, 117.

[26] Z. H. Nie and E. Kumacheva, *Nat. Mater.*, 2008, *7*, 277.

[27] E. J. Menke, M. A. Thompson, C. Xiang, L. C. Yang and R. M. Penner, *Nat. Mater.*, 2006, *5*, 914.

[28] A. Sinitskii and J. M. Tour, *J. Am. Chem. Soc.*, 2010, *132*, 14730.

[29] B. Hatton, L. Mishchenko, S. Davis, K. H. Sandhage and J. Aizenberg, *Proc. Natl. Acad. Sci. U. S. A.*, 2010, *107*, 10354.

[30] T. S. Mentzel, D. D. Wanger, N. Ray, B. J. Walker, D. Strasfeld, M. G. Bawendi and M. A. Kastner, *Nano Lett.*, 2012, *12*, 4404.

[31] P. V. Dudin, P. R. Unwin and J. V. Macpherson, *J. Phys. Chem. C*, 2010, *114*, 13241.

[32] S. Manne, P. K. Hansma, J. Massie, V. B. Elings and A. A. Gewirth, *Science*, 1991, *251*, 183.

[33] D. M. Kolb, R. Ullmann and T. Will, *Science*, 1997, *275*, 1097.

[34] P. V. Dudin, M. E. Snowden, J. V. Macpherson and P. R. Unwin, *ACS Nano*, 2011, *5*, 10017.

[35] Y. Lu, Z. Tu and L. A. Archer, *Nat. Mater.*, 2014, *13*, 961.

[36] R. C. Hayward, D. A. Saville and I. A. Aksay, *Nature*, 2000, *404*, 56.

[37] P. Y. Chiou, A. T. Ohta and M. C. Wu, *Nature*, 2005, *436*, 370.

[38] H. Hwang, H. Chon, J. Choo and J.-K. Park, *Anal. Chem.*, 2010, *82*, 7603.

[39] S. Ota, S. Wang, Y. Wang, X. Yin and X. Zhang, *Nano Lett.*, 2013, *13*, 2766.

[40] D. J. Harrison, G. S. Calabrese, A. J. Ricco, J. Dresner and M. S. Wrighton, *J. Am. Chem. Soc.*, 1983, *105*, 4212.

[41] G. S. Calabrese, M. S. Lin, J. Dresner and M. S. Wrighton, *J. Am. Chem. Soc.*, 1982, *104*, 2412.

[42] C. M. Gronet, N. S. Lewis, G. W. Cogan, J. F. Gibbons, G. R. Moddel and H. Wiesmann, *J. Electrochem. Soc.*, 1984, *131*, 2873.

[43] R. H. Micheels, *Appl. Phys. Lett.*, 1981, *39*, 418.

[44] T. L. Rose, *Appl. Phys. Lett.*, 1983, *42*, 193.

[45] T. Inoue, A. Fujishima and K. Honda, *J. Electrochem. Soc.*, 1980, *127*, 1582.

[46] S.-H. Huang, H.-J. Hsueh and Y.-L. Jiang, *Biomicrofluidics*, 2011, *5*, 034109.

[47] W. Kern and D. A. Puotinen, *RCA Rev.*, 1970, *31*, 187.

[48] T. Hattori, K. Watanabe, M. Ohashi, M. Matsuda and M. Yasutake, *Appl. Surf. Sci.*, 1996, *102*, 86.

[49] K. Saito, M. Matsuda, M. Yasutake and T. Hattori, *Jpn. J. Appl. Phys.*, 1995, *34*, L609.

[50] M. Matsumura, Y. Sakai, S. Sugahara, Y. Nakato and H. Tsubomura, *Sol. Energy Mater.*, 1986, *13*, 57.

[51] N. Chazalviel and P. Allongue, *J. Am. Chem. Soc.*, 2011, *133*, 762.

[52] G. P. Kissling, D. O. Miles and D. J. Fermin, *Phys. Chem. Chem. Phys.*, 2011, *13*, 21175.

[53] C. R. Bradbury, J. Zhao and D. J. Fermin, *J. Phys. Chem. C*, 2008, *112*, 101530.

[54] J.-Y. Lee, J. G. Lee, S.-H. Lee, M. Seo, L. Piao, J. H. Bae, S. Y. Lim, Y. J. Park and T. D. Chung, *Nat. Commun.*, 2013, *4*, 2766.

[55] M. T. Kelly, J. K. M. Chun and A. B. Bocarsly, *J. Phys. Chem. B*, 1997, *101*, 2702.

[56] J. Velmurugan, D. Zhan and M. V. Mirkin, *Nat. Chem.*,

2010, *2*, 498.

[57] A. Barkschat, H. Tributsch and J. K. Dohrmann, *Sol. Energy Mater. Sol. Cells*, 2003, *80*, 391.

[58] S. Thiyagu, Z. W. Pei and M. S. Jhong, *Nanoscale Res. Lett.*, 2012, *7*, 1.

[59] B. Seger, T. Pedersen, A. B. Laursen, P. C. K. Vesborg, O. Hansen and I. Chorkendorff, *J. Am. Chem. Soc.*, 2013, *135*, 1057.

3. Light-Driven Highly Selective Conversion of CO_2 to Formate by Electrosynthesized Enzyme/Cofactor Thin Film Electrode

3.1 Introduction

The conversion of CO_2 into commodity chemicals has been received much attention because it can also reduce atmospheric CO_2 by replacing existing fossil fuel-based synthesis [1]. To date, research on the highly selective and energy-efficient electrochemical conversion of CO_2 has been inclined to surface optimization of metal-based electrodes or electrolytes, which presumably have advantages such as their stability and cost, enabling mass production [2]. Some metal-based catalysts, for example, Cu_2O, enable CO_2 reduction at comparatively low potentials (−0.5 V vs RHE) than existing catalysts [2,3]. However, CO_2 conversion in practice still requires much greater advance for the economic and environmental concerns; higher Faradaic efficiency, more selective production of desired product under mild conditions, and better stability with cheaper materials and lower consequential energy consumption for sustainable production [4,5].

Photosynthetic systems of living organisms and their

components in nature have evolved to have excellent functional structures for atmospheric CO_2 reduction [6]. Therefore it is no wonder that enzymatic CO_2 reduction has been extensively examined as a promising approach for CO_2 utilization by mimicking the biological CO_2 fixation cycles in plants and some prokaryotes [6,7]. Recently, combined systems of enzymatic electrodes and photoelectrochemical (PEC) reactions have been suggested for artificial photosynthesis [7,8-11]. Although a few pioneering works showed good selectivity for single product owing to the inherent specificity of enzymes [9], there are still a couple of issues to address, one of which is instability of the biocatalytic components [12]. The three-dimensional (3D) structure of enzyme, which plays a pivotal role in efficient and selective redox catalysis, is vulnerable to its artificial reaction environments [13]. To improve the short lifetime of enzyme-based electrodes, much efforts have been made on the development of inter/intra enzymatic matrix such as functionalized polymers, e.g., chitosan, Nafion, and polyamines [12,14]. In addition, electrical contact between electrode and redox centers inside the enzymes surrounded by insulating proteins is key challenges in tailoring enzymatic electrode. Dissolving diffusional electron mediators in electrolyte solutions, one of the most common methods, can be another origin of low stability of bioelectrode because of

their vanishing electrochemical reversibility during the redox process [13]. In addition, the redox polymers or the chemically modified enzyme containing electron relay groups in itself were used to generate the electrical wiring between the biological components and electrodes [15,16].

Here, we report a compactly organized bioelectrode for the highly selective reduction of CO_2 to formate at the electrochemically synthesized polydopamine (PDA) thin films copolymerized with an enzyme (E, FDH) and its cofactor (C, NADH) as an electron mediator (Fig. 3-1). We chose PDA as a matrix for enzyme immobilization because of its multifunctionality; that is, it is biocompatible and has good charge transfer capabilities [17]. The PDA layer on the electrode is expected to meet the essential conditions, i.e., facilitating electron transfer and stabilizing enzyme for prolonged lifetime [17-19]. As analyzed by the voltammograms, both enzyme and cofactor are closely linked to the PDA network during the electropolymerization of dopamine (DA) monomers [20,21]. Furthermore, we have designed a bioinspired light to fuel production system using the PEC oxygen evolution reaction (OER), which is a major renewable power sources [22,23]. The system consists of nanoporous cobalt phosphate/bismuth vanadate ($CoP_i/BiVO_4$) photoanode and EC-incorporated PDA bioelectrode to complete the sustainable energy-conversion system without

external bias.

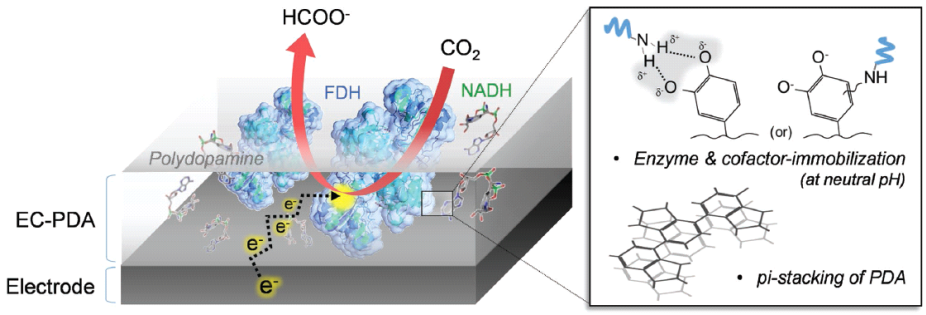

Fig. 3-1 Schematic illustration of 3D structure and proposed formation mechanism of EC-PDA thin film-coated biocathode.

3.2 Experimental

3.2.1. Materials and reagents

Formate dehydrogenase from Candida boidinii (13.3 U mg^{-1} protein), β-nicotinamide adenine dinucleotide, reduced sodium salt hydrate (NADH), dopamine hydrochloride and Nifion 117 membrane (thickness 0.007 in) were purchased from Sigma-Aldrich. Bismuth nitrate pentahydrate ($Bi(NO_3)_3 \cdot 5H_2O$, ≥98.0%), vanadyl acetylacetonate ($VO(acac)_2$, 98%), and cobalt nitrate hexahydrate ($Co(NO_3)_2 \cdot 6H_2O$, ≥98.0%) were purchased from Sigma-Aldrich and used as received. Dimethylsulfoxide (DMSO) and ethylene glycol solution were purchased from Daejung Chemicals.

3.2.2. Electrochemical preparation of electrodes

To fabricate the EC-PDA biocathode, the surface of the glassy carbon electrode (GCE, 0.3 × 2.5 × 2.5 cm^3, ALS) was polished with 0.3 and 0.05 μm alumina (Buehler, Lake Bluff) successively. After cleaning, 0.5 V was applied to fixed area of the GCE in the sodium phosphate buffer (0.1 M, pH 6.0) containing 1 mM DA monomer, 1 mM NADH, and 1 mg mL^{-1} FDH. An Ag/AgCl (in 3 M NaCl, 0.209 V vs NHE) and a platinum wire were used for reference and

counter electrodes, respectively, for electrochemical polymerization.

The photoanode, $BiVO_4$, was fabricated according to the previously reported method; briefly, for deposition of Bi, −1.8 V (vs Ag/AgCl) was applied at FTO for 60 s followed by a resting time for 2 s at 0 V (vs Ag/AgCl) in ethylene glycol solutions containing 20 mM $Bi(NO_3)_3$. This cycle was repeated eight times were optimum number of pulses that let total charge of 320 mC cm^{-2} pass (Fig. 3-2). To convert Bi into $BiVO_4$, 200 μL of 150 mM $VO(acac)_2$ in DMSO was dropped to the as-deposited Bi electrode and then annealed at 450 ℃ for 2 h in air (ramping rate = 1.8 ℃ min^{-1}). After annealing, residual V_2O_5 was removed by immersion of electrode in stirred 1 M NaOH solution for 30 min to make intrinsic $BiVO_4$ surface exposed to outside. The oxygen evolution catalyst, CoP_i, was electrodeposited onto $BiVO_4$/FTO by applying 0.3 V (vs Ag/AgCl) under simulated AM 1.5 illumination from back side of the electrode. The photoassisted CoP_i electrodeposition was optimized at about 42 mC cm^{-2}. The CoP_i electrodeposition bath was filled with 0.5 mM $Co(NO_3)_2 \cdot 6H_2O$ in 0.1 M sodium phosphate buffer (pH 7.0) as shown in Fig. 3-3. The final film was rinsed with DI water before use.

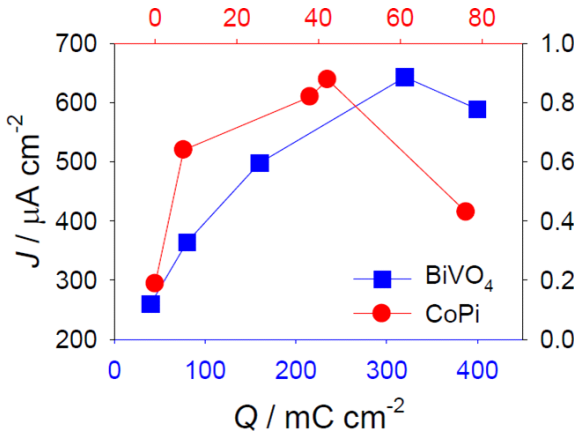

Fig. 3-2 Optimization of photoanode. Current density (at 0.8 V vs. Ag/AgCl) of photoanodes as a function of the total charge passed during Bi electrodeposition onto the FTO electrode (blue) and the amounts of CoPi loading (red) at the optimized $BiVO_4$ photoelectrode. The optimized total charge values for Bi and CoP_i deposition was 320 and 42.2 mC cm^{-2}, respectively.

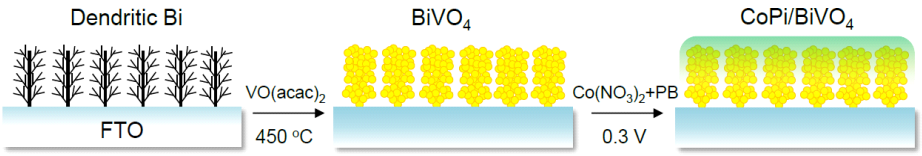

Fig. 3-3 Preparation procedure of CoP_i-electrodeposited $BiVO_4$ photoanode ($CoP_i/BiVO_4$).

3.2.3. Regeneration of NADH

Reduction of NAD^+ was monitored with 1 mM NAD^+ in 0.1 M sodium phosphate buffer (pH 7.0) at −0.8 V (vs. Ag/AgCl) for 1 hour. The absorbance of NADH at 340 nm was recorded to determine the concentration of generated NADH. Turn over frequencies were calculated in mole of NADH produced per hour.

3.2.4. Isotope-tracer experiments

^{13}C-NMR data was acquired after the electrolysis in $^{13}CO_2$-saturated solutions. The electrolysis conditions was identical with CO_2 reduction reaction for the HPLC analysis. The working electrode was EC-PDA biocathode and the counter electrode was Pt wire. The applied potential was −0.5 V (vs. Ag/AgCl) and the electrolysis was conducted for 4 hours. The NMR spectra were recorded on a Bruker Avance 600 instrument (at 600 MHz for $^{13}CNMR$) equipped at National Instrumentation Center for Environmental Management (NICEM) of Seoul National University.

3.2.5. Determination of formate concentration

The amount of formate in the cathodic chamber was generated by high performance liquid chromatography (HPLC) using a Dionex Ultimate 3000 (Thermo Scientific, USA) equipped with an Aminex 87H column (Bio-Rad, USA)

at 40 ℃ using a bolum heater module (Agilent G1316 B). The mobile phase consisted of 0.01 N H_2SO_4 and flow rate was 0.5 mL min^{-1}. The HPLC system was connected to a refractive index (RI) detector. UV-Vis spectra were registered at 210 nm.

3.2.6. Mott-Schottky analysis to calculate the flatband potential of $BiVO_4$

Capacitance data for Mott-Schottky plot were measured at a sinusoidal modulation of 10 mV at frequencies of 0.5, 0.75, and 1 kHz under dark conditions. The calculated E_{FB}, −0.53 ± 0.01 V (vs. Ag/AgCl), was obtained by averaging the values from three independent measurements. The exposed geometric photoelectrode area was 0.28 cm^2. The electrolyte was 0.1 M phosphate buffer containing 1 M sodium sulfite and the same three-electrode cell was used.

3.2.7. Calculation of light conversion efficiency to chemical energy

The value of light conversion efficiency to chemical energy was calculated by dividing the combustion heat of formic acid produced by the total energy of the simulated solar AM 1.5 G illumination:

$$= \left[\begin{array}{c} (mmol\,cm^{-2}) \times (270\,kJmol^{-1}) \\ \lfloor \quad (mWcm^{-2}) \times A\ (cm^2) \end{array} \right]_{M1.5G} \times 100$$

where the 270 kJ mol^{-1} is the molar heat of combustion of formic acid (ΔH_C), I the incident illumination intensity (100 mW cm^{-2} in this work) and electrode area (A) the 1.7 cm^2.

3.2.8. Instrumentation

A home-built solar simulator that had 150 W Xenon arc lamp with AM 1.5 G filter was used as a light source for photoelectrochemical CO_2 reduction experiments. The light intensity was calibrated to 100 mW cm^{-2} before the experiments with a radiometer (Solar light, PMA-2100) and a pyranometer (PMA-2144). All potential except for biocathode/photoanode-combined system were measured against an Ag/AgCl reference electrode (3.0 M NaCl, Bioanalytical System, Inc.). Electrochemical experiments were conducted using CHI 601C electrochemical workstation except for Mott-Schottky measurements conducted by Gamry Reference 600. The chopping illumination was made with 300CD optical chopper system (Scitec Instruments). Atomic force microscope analysis was conducted by the contact mode in NanoStation II model (Surface Imaging Systems). The top and cross-sectional view of $CoP_i/BiVO_4$ photoanode were taken using SUPRA 55VP (Carl Zeiss) at accelerating voltage of 2 kV in National Instrumentation Center for Environmental Management of Seoul National University. The XRD analysis was carried out using a high resolution X-ray

diffractometer (Bruker D8 DISCOVER) at the Seoul National University National Center for Inter-University Research Facilities (NCIRF). The amount of formate was determined using a Gas Chromatography (GC, YoungLin-6000) with a packed MolSieve 5A column (Supelco) and flame ionization detector (FID) and High Performance Liquid Chromatography (HPLC, Ultimate3000, Thermo) with Gel H crosslinked column (Supelco) and UV/vis detector.

3.3 Results and Discussion

3.3.1. Fabrication of polydopamine-based enzyme/cofactor thin film-covered biocathode

The biocathode consisted of the PDA and enzyme/cofactor (EC) immobilized on the electrode surface (Fig. 3-4). First, we checked the redox characteristics of DA with and without EC by cyclic voltammetry (0 to 0.5 V) in 0.1 M sodium phosphate buffer (pH 6.0) (Fig. 3-5). The cyclic voltammograms of the DA monomer solutions containing NADH show that the oxidation currents are significantly enhanced, while NADH itself is oxidized slowly and irreversibly at a bare glassy carbon electrode (GCE) surface (Fig. 3-6A). FDH alone gives a negligible oxidation wave by itself, but enhances the electrochemical oxidation of DA as presented in Fig. 3-6B. In contrast, the presence of both NADH and FDH increased oxidative peak current with a little positive shift of peak potential. These results indicate that both NADH and FDH facilitate the electrochemical oxidation of DA. As for reduction peak, FDH caused a negative shift, whereas the presence of NADH makes it back to less negative potential (Fig. 3-5). Concerning the voltammetric behavior of DA and the influence of NADH and FDH, the carbonyl groups in the quinoidal moieties presumably play a

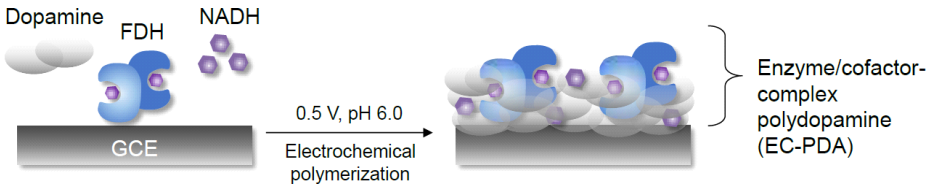

Fig. 3-4 Electrochemical fabrication procedure of Enzyme (E,FDH)/cofactor (C,NADH)-combined polydopamine (EC-PDA)-electropolymerized biocathode

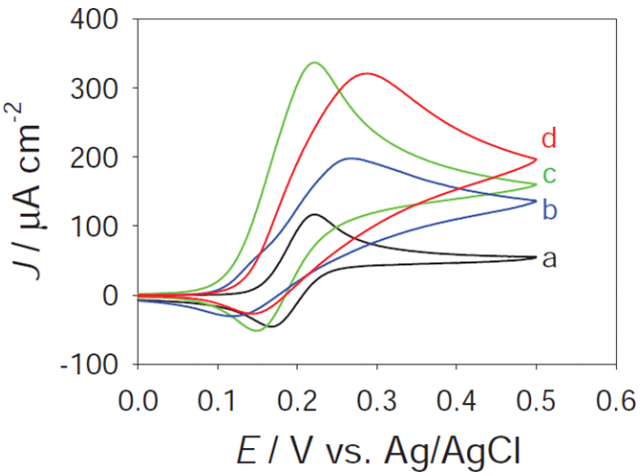

Fig. 3-5 Electrochemical experiments demonstrating incorporating of FDH and NADH into the PDA layer during electropolymerization. Cyclic voltammograms of a) DA only, b) FDH+DA, c) NADH+DA, and d) FDH+NADH+DA solutions (0.1 M sodium phosphate buffer, pH 6.0; scan rate 20 mV s^{-1}) to compare with voltammograms measured during DA electropolymerization.

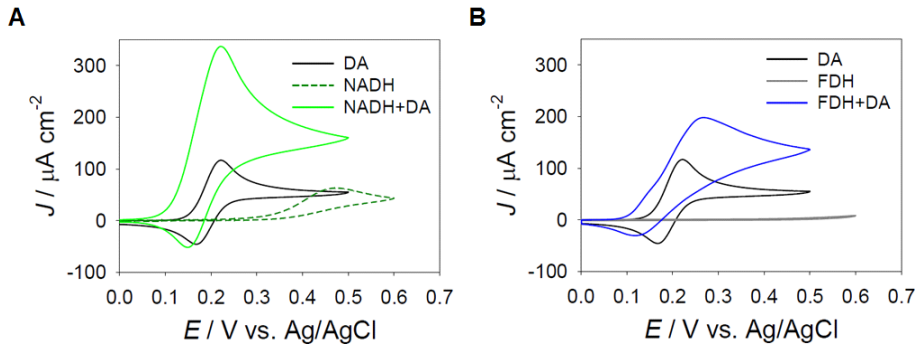

Fig. 3-6 Cyclic voltammograms of (A) NADH+DA and (B) FDH+DA solutions to compare with voltammograms measured during dopamime (DA) electropolymerization (0.1 M sodium phosphate buffer, pH 6.0; scan rate 20 mV s^{-1}). Electrochemical redox characteristics of NADH and FDH also shown in panel (A) and (B), respectively.

certain role. The quinoidal moiety of DA, which has similar structure to ubiquinone in biological system, catalyzes the oxidation of NADH efficiently as indicated by substantial diminution of overpotential [24]. Importantly, one-electron oxidation of cofactor, NADH dissolved in electrolyte, yields unstable cation radical intermediates to be likely to form electrochemically inactive dimers, leading to drop of its turnover number [25]. That is why electrochemical reduction of NAD^+ at bare GCE requires much higher overpotential (at −1.18 V, see Fig. 3-7) than their inherent reduction potentials (−0.56 V vs SCE at pH 7.0) [25]. Meanwhile, reduction current at PDA-coated electrode increased at positive potential and its turnover frequency grew ~30% than bare GCE in 0.1 M sodium phosphate buffer (pH 7.0) containing NAD^+ (Fig. 3-8). Accordingly, NADH-incorporated enzyme electrode must minimize post-electrochemical reaction among oxidized NADH (NAD^+). The quinoidal moiety of DA hampers dimerization so as to facilitate electron transfer between NADH and the electrode [24]. It is not surprising that conjugated NADH/PDA scaffold plays a role of redox active polymer surrounding enzyme with structural stability as if in biological state.

In nature, the adenosine moiety of a cofactor NADH is ready to interact with amino acid residues (Thr282, Asp308,

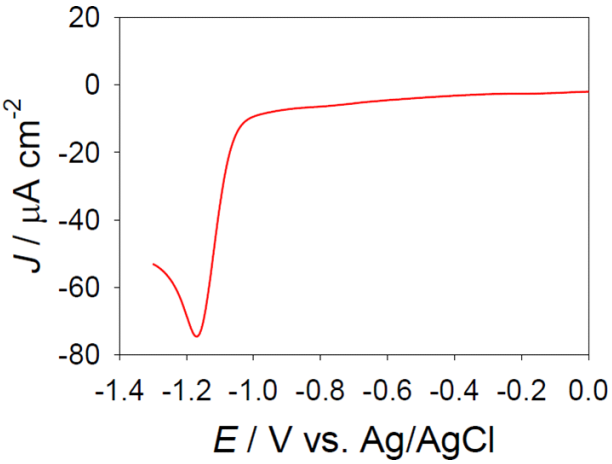

Fig. 3-7 Reduction current with NAD^+ at bare GCE (0.1 M sodium phosphate, pH 7.0).

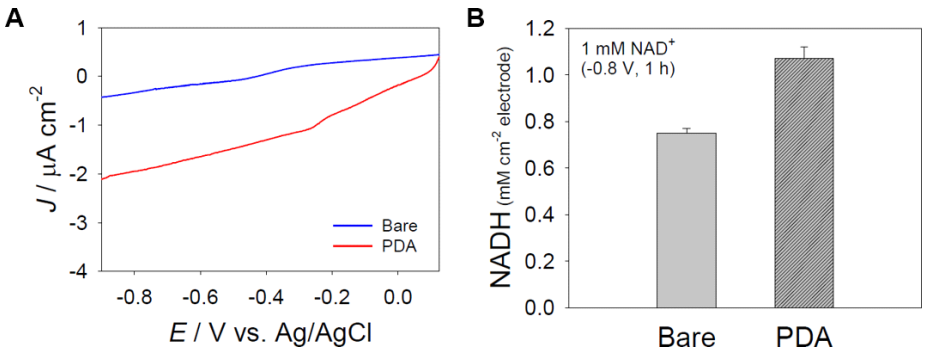

Fig. 3-8 (A) Reduction currents with 1 mM NAD^+ at bare GCE and PDA-coated GCE (0.1 M sodium phosphate, pH 7.0). (B) The regeneration yields of NADH by bare and PDA-coated electrode were determined after 1 h reaction. A potential of −0.8 V (vs. Ag/AgCl) was applied in 0.1 M sodium phosphate buffer (pH 7.0) with 1 mM NAD^+.

Ser334, and Gly335) located in the active site via hydrogen bonds and stabilize the positively charged cation radical intermediates [26]. In the proposed system, NADH and FDH as electron mediator and reaction catalyst enzyme, respectively, participate in the functional film on the electrode without covalent linkage. Negatively charged PDA at neutral pH as a result of deprotonation of phenolic group gives favorable for keeping NAD^+ within the PDA film. Molecular structures of NADH and PDA indicate the presence of numerous hydrogen bonds that form 3D network. In PDA itself, $\pi-$stacking secures robust matrix. Besides, indole rings of dopamine efficiently inhibit dimerization to ensure regeneration of NAD^+. These multiple factors are orchestrated to create exceptionally favorable environment in PDA-NADH-FDH composite film (Fig. 3-1) [27-29].

3.3.2. Performance of biocathode for CO_2 reduction

The PDA incorporating the EC complex was electropolymerized at a constant potential (at 0.5 V) on the electrode surface (Fig. 3-9) [21]. Once the PDA film is formed by oxidative electropolymerization, it appears that FDH serves as a reaction catalyst while NADH mediateselectron transfer, favoring reduction of the PDA film. As shown in Fig. 3-10, the much lower capacitive

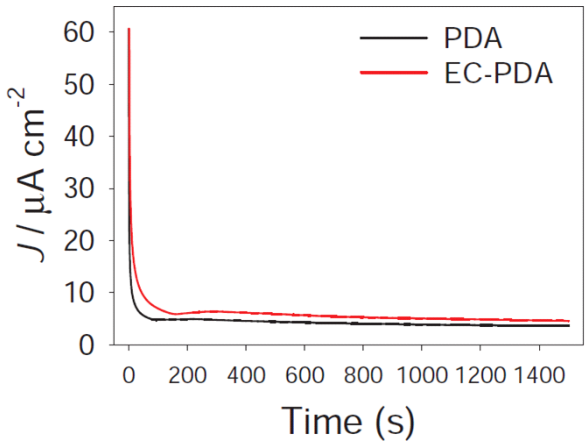

Fig. 3-9 Current density during the electrochemical polymerization of the PDA and EC-PDA layer (at 0.5 V vs Ag/AgCl).

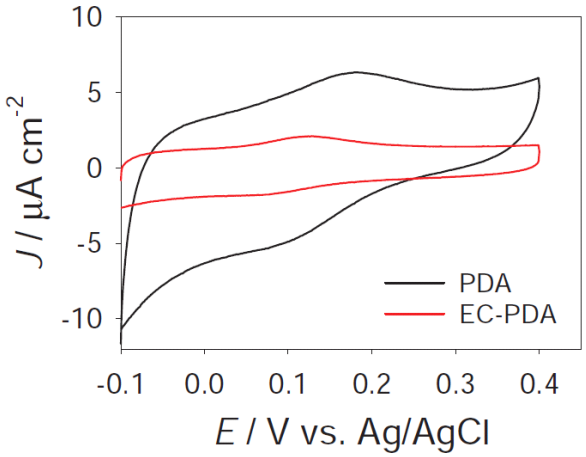

Fig. 3-10 Cyclic voltammograms of PDA and EC-PDA coated GCE in 0.1 M sodium phosphate buffer (pH 7.0; scan rate 25 mV s^{-1}).

current of the EC-PDA layer in comparison to PDA indicates that denser and/or thinner film was created when EC was incorporated into the PDA film. This supports the idea that NADH and FDH in the PDA layer are closely associated with the PDA backbone creating an unusually compact multifunctional film. The scan rate dependence of the peak current reveals that the redox peak originates from the EC-PDA layer immobilized on the GCE surface (Fig. 3-11). The co-existence of E and C is essential for CO_2 reduction because NADH serves as an electron shuttle between FDH and the GCE surface (Fig. 3-12) [30].

The EC-PDA layer on GCE was optimized by controlling the time for electropolymerization because PDA continues to grow with elongating electropolymerization time [21,31]. The maximum current density of CO_2 reduction at the EC-PDA biocathode (at −0.5 V) was observed and optimal time condition for electropolymerization was determined as shown in Fig. 3-13. Based on the previous report investigating the effects of potential duration on the PDA layer thickness [21], we expect that our optimized EC-PDA layer is less than 10 nm. Our expectation is further proved by the morphology of protruding enzymes shown in AFM image (Fig. 3-14). The morphological property of EC-PDA imply that globular and dimeric forms of FDH (364 amino acids, ~5 nm diameter) [32] with NADH successfully embedded in

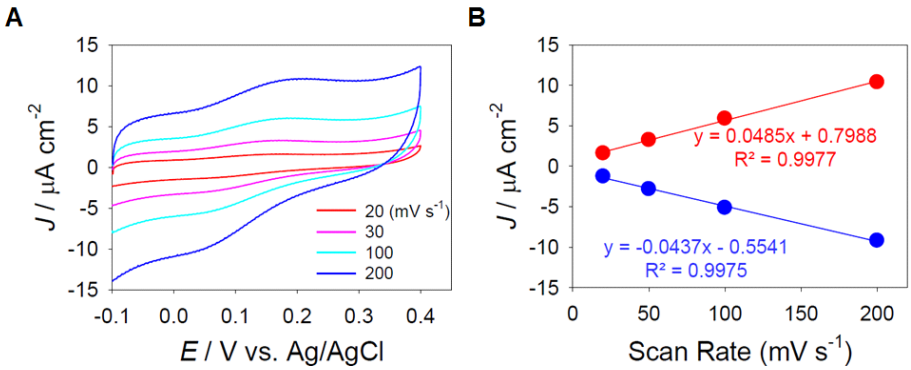

Fig. 3-11 Electrochemical characterization of EC-PDA coated GCE. a) Cyclic voltammograms of the EC-PDA at various scan rates (20, 50, 100, and 200 mV s^{-1}). b) Plots of peak current vs. scan rate.

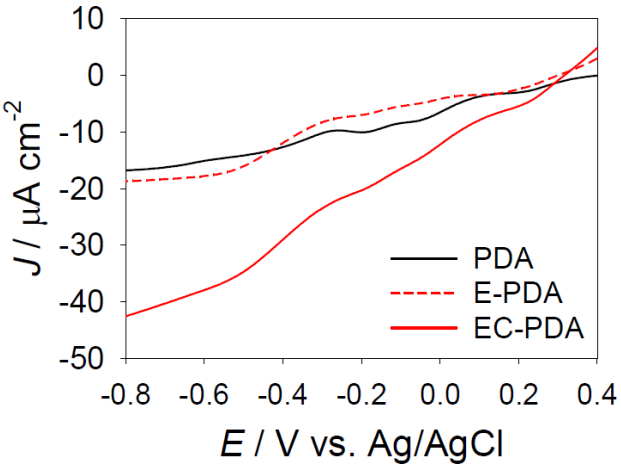

Fig. 3-12 Current potential characteristics of PDA, E-PDA and EC-PDA coated GCEs under CO_2 atmosphere.

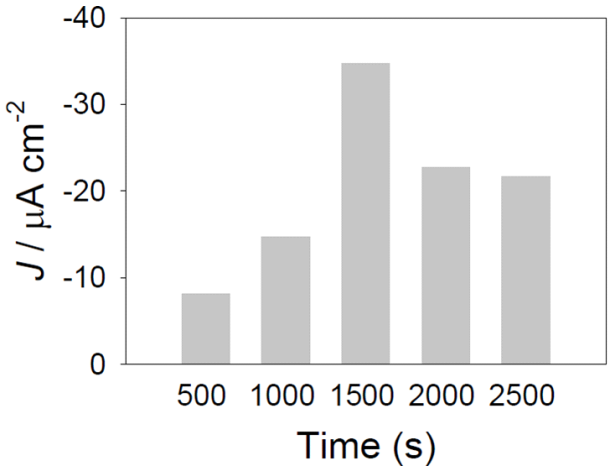

Fig. 3-13 Maximum current densities of the EC-PDA biocathode at −0.5 V (vs. Ag/AgCl) as a function of different times of electropolymerization (500 to 2,500 s). Measurements were performed in 0.1 M sodium phosphate (pH 7.0) solution under CO_2 atmosphere at −0.5 V vs Ag/AgCl.

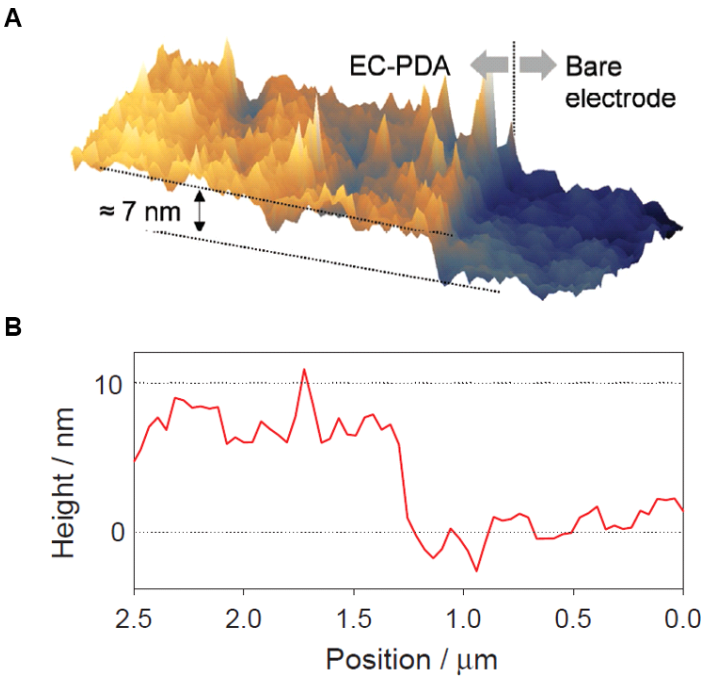

Fig. 3-14 (A) 3D image and (B) height profile of the EC-PDA bioelectrode generated from atomic force microscopy analysis.

PDA as illustrated in Fig. 3-1. The EC-PDA covered GCE gave higher current at -0.5 V than a PDA-coated GCE in a CO_2-saturated solution in comparison to N_2 atmosphere (Fig. 3-15). In addition, ^{13}C-NMR and HPLC analysis of the products from the biocathode at -0.5 V under $^{13}CO_2$ saturation ensured the formation of $H^{13}COO^-$ with nearly 100% faradaic efficiency, supporting that the carbon source for formate was the CO_2 molecules (Fig. 3-16).

To characterize the electrocatalytic activity of biocathode, EC-PDA voltammograms from a glassy carbon (GC) rotating disk electrode (RDE) were recorded at different rotating speeds. The speed of the RDE controls convective mass transport rate of CO_2 from bulk solution to the electrode (Fig. 3-17). Without convection (no rotation), the onset potential and peak potential were -0.4 V and -0.65 V, respectively (inset of Fig. 3-17). In contrast, when CO_2 was supplied effectively to the EC-PDA layer at a rotation speed of 2000 rpm, the diffusion-controlled current which was clear without convection, was disappeared. Nonetheless, the faradaic current was increased over gaining rotation speed. This typical electrochemical behavior shown in RDE experiments indicating that the catalytic activity of the enzymes immobilized on the GCE is sufficient to produce a higher current in response to the increasing convective transport of reactants to the electrode [8,33]. On the basis

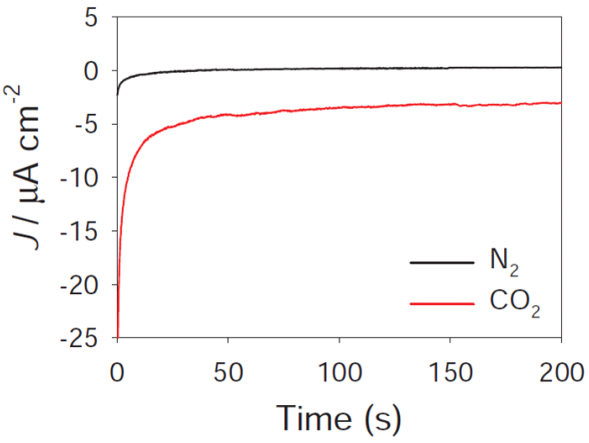

Fig. 3-15 Current response of the optimized EC-PDA biocathode with or without CO_2 gas at −0.5 V (vs. Ag/AgCl).

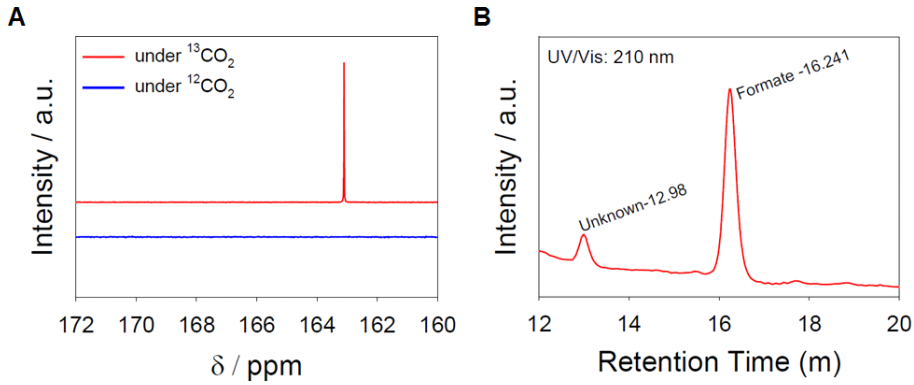

Fig. 3-16 (A) ^{13}C-NMR and (B) HPLC spectra of a reacted solution (0.1 M sodium phosphate, pH 7.0) from a tracer experiment utilizing $^{13}CO_2$.

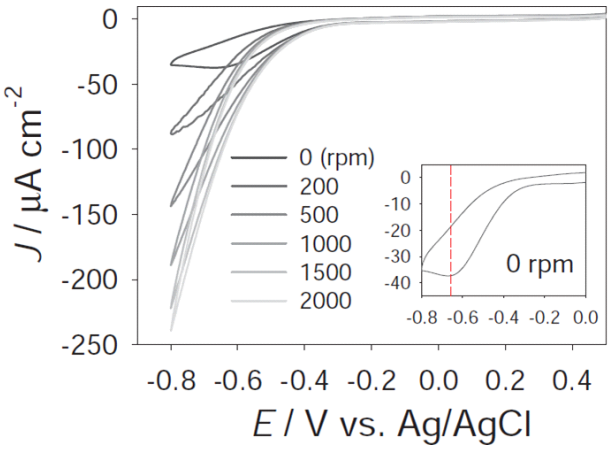

Fig. 3-17 Cyclic voltammograms measured with a GC RDE coated with EC-PDA in the presence of CO_2 (scan rate 25 mV s^{-1}).

of the RDE experiments, the proposed EC-PDA electrode is expected to generate higher faradaic current upon higher CO_2 concentrations, and no significant passivation of the electrode itself was observed during the period of continuous monitoring.

To evaluate long-term stability of the EC-PDA biocathode, the current density of CO_2 saturated buffer was periodically recorded by performing 30 min discharge at −0.5 V (vs Ag/AgCl) for 16 d. As shown in Fig. 3-18, the biocathode delivered −1.2 μA cm^{-2} after 16 d, which represents ~60% of its initial electrocatalytic activity and constitutes the highest lifetime reported until now for an electrochemical reduction of CO_2 using enzymatic electrochemical systems. This is a remarkable result because conventional enzymatic electrodes normally suffer from a decrease in enzyme activity [13]. Therefore, most enzymatic electrode systems try to immobilize as many enzymes as possible in thick matrices to ameliorate the effects of chronic deterioration of the enzyme layers. In contrast, the electrosynthesized PDA in this study seems to grab NADH and FDH tightly in its thin and conformal film, the thickness of which is comparable to the diameter of FDH. In this system, NADH serves as a cofactor or an electron mediator that should relay electron from underlying electrode surface to the redox active center inside FDH [34]. Cofactor NADH is predicted to reside in

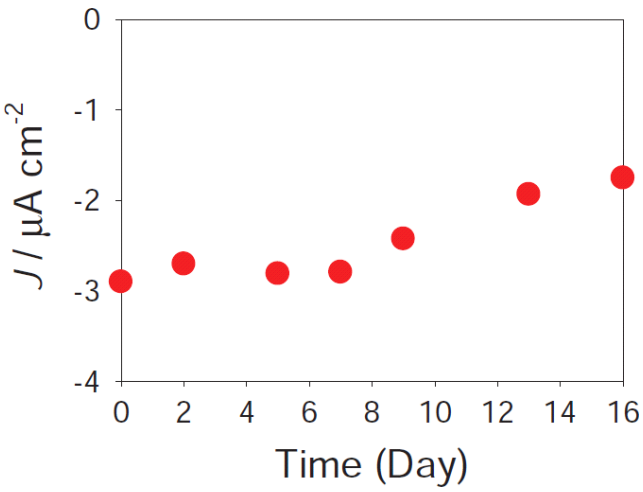

Fig. 3-18 Long-term stability of the EC-PDA biocathode. Measurements were performed in 0.1 M sodium phosphate (pH 7.0) solution under CO_2 atmosphere at −0.5 V versus Ag/AgCl.

the deep cleft of the active site residues of the enzyme [32]. Accordingly, charge transfer between FDH and NADH in the vicinity of the active site should occur swiftly [15,16]. Owing to several nanometer thickness of the EC-PDA film, the distance that electrons should transport among NADH might be minimized so as to remarkably prevent inevitable loss of faradaic charges. Besides, there is almost no need for both reactant and product to permeate the film so that reactant can freely access to enzyme and product can diffuse out in the film-solution interface.

3.3.3. Performance $CoP_i/BiVO_4$ photoanode for water oxidation

The photoanode for water oxidation was composed of a $BiVO_4$ layer. This was prepared by following previous literature methods; that is a solution-processed method that consisted of electrodeposition and chemical treatment (Fig. 3-3). As shown in the top and cross-sectional view of scanning electron microscope (SEM) images (Fig. 3-19), the final film with an average thickness of about 1 μm is composed of $BiVO_4$ particles of several hundred nanometers in diameter. The $BiVO_4$ coated fluorine doped tin oxide (FTO) electrode was confirmed by X-ray diffraction pattern (Fig. 3-20). The flatband potential (E_{FB}) calculated by the Mott-Shottky plots (Fig. 3-21) was about -0.53 ± 0.01 V

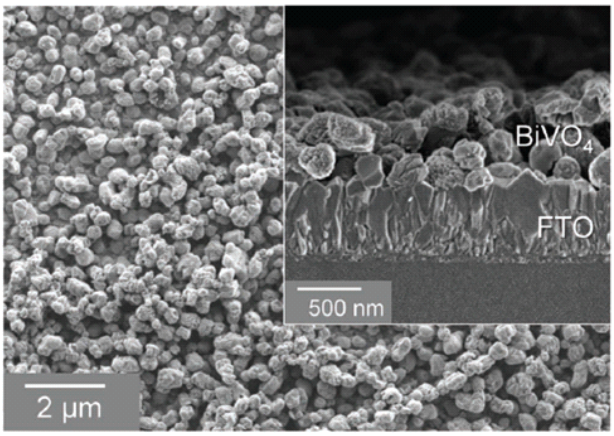

Fig. 3-19 The top and cross-sectional view of $CoP_i/BiVO_4$ photoanode at the SEM images.

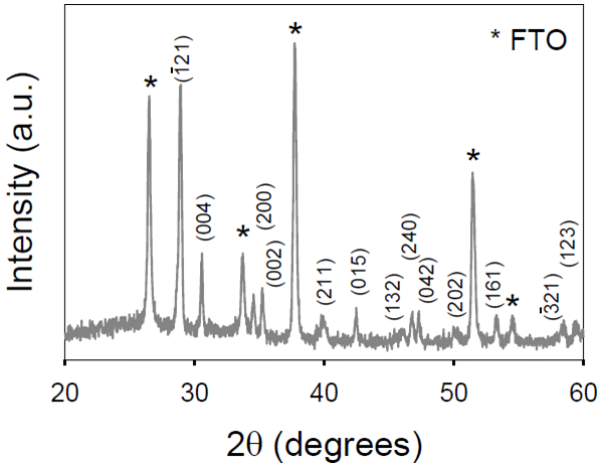

Fig. 3-20 X-ray diffraction pattern of the $BiVO_4$ coated FTO electrode.

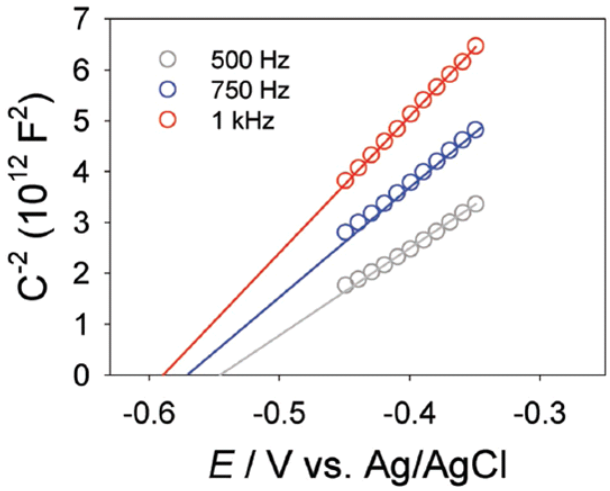

Fig. 3-21 Mott-Schottky plot of bare $BiVO_4$ measured in 0.1 M sodium phosphate buffer (pH 7.0) containing 1 M sulfite ions as a sacrificial reagent at an applied frequency of 500, 750, and 1000 Hz.

(vs Ag/AgCl) at pH 7.0 buffer solutions containing 1 M sulfite as a sacrificial reagent. This value, ~0.1 V versus RHE, agrees well with the previous reports [39,43]. From the calculated E_{FB}, the conduction band edge position (E_C) corresponds to −0.6 V (vs Ag/AgCl) by assuming the E_C is located at 100 mV above the E_{FB} [35]. This assumption is necessary because of the ambiguity of the surface area originating from the nanoparticulate nature of the $BiVO_4$ film. The conduction band edge is at slightly more negative than the formal potential of the NAD^+/NADH (~−0.53 V vs Ag/AgCl at neutral pH). This indicates that the $BiVO_4$ can not only oxidize the water but also play a role as electron supplier for cathodic reaction, i.e., CO_2 reduction.

To increase the photovoltage, we electrodeposited CoP_i, a renowned oxygen evolution catalyst that mimics the reaction center in photosynthetic system II (PS II) [36], on the $BiVO_4$ layer until a charge of about 42 mC cm^{-2} was achieved (Fig. 3−2). Linear sweep voltammograms for water oxidation were recorded in 0.1 M sodium phosphate buffer (pH 7.0) at 25 mV s^{-1} under constant simulated AM 1.5 G illumination. Fig. 3−22 shows that current density from $CoP_i/BiVO_4$ is much larger than that of $BiVO_4$ layer alone as expected. A linear sweep voltammogram measured under chopped illumination (1.5 Hz) at a scan rate of 100 mV s^{-1} almost coincided with the voltammogram under constant

illumination. This indicates that photogenerated holes are efficiently transferred to electrolyte solutions via water oxidation at the $CoP_i/BiVO_4$ interface [37]. The functional tandem processes of the combination of $CoP_i/BiVO_4$ photoanode and EC−PDA biocathode, which mimics natural photosynthesis, depicted in Fig. 3−23. The self−biased light energy for high performance CO_2 reduction described here is powered by an n−type semiconductor, $BiVO_4$, which has a higher absorption coefficient and better band edge alignment than other metal oxide semiconductors [38]. The catalyst, CoP_i can substantially reduce the kinetic overpotential for the OER and ensures that the electrode is stable at wide range of electrochemical potentials in solutions near neutral pH [38,39]. Our results showed that the valence band edge of $BiVO_4$ (1.9 V vs Ag/AgCl) is suitable for the oxidation of water molecules (0.61 V vs Ag/AgCl at pH 7.0), and the measured conduction band edge position (−0.6 V vs Ag/AgCl) of $BiVO_4$ is more negative than the formal potential of the NADH (−0.53 V vs Ag/AgCl), which is a redox cofactor for enzymatic CO_2 reduction, in EC−PDA biocathode. It suggests that the band structure of the device components satisfies minimum conditions for self−biased CO_2 conversion to formate. In addition, our biocathode shows highly selective electrocatalytic activity and minimal electron transfer resistance of PDA−NADH−FDH combination as shown here.

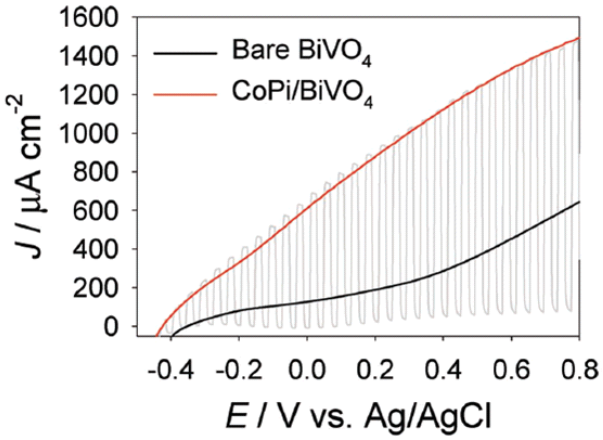

Fig. 3-22 Linear sweep voltammograms (scan rate 25 mV s^{-1}) of bare $BiVO_4$ and $CoP_i/BiVO_4$ on FTO electrodes under visible light irradiation using a 150 W Xe Arc lamp (light intensity adjusted to 100 mW cm^{-2}) equipped with cut-off filter at $\lambda > 420$ nm) in 0.1 M sodium phosphate buffer (pH 7.0).

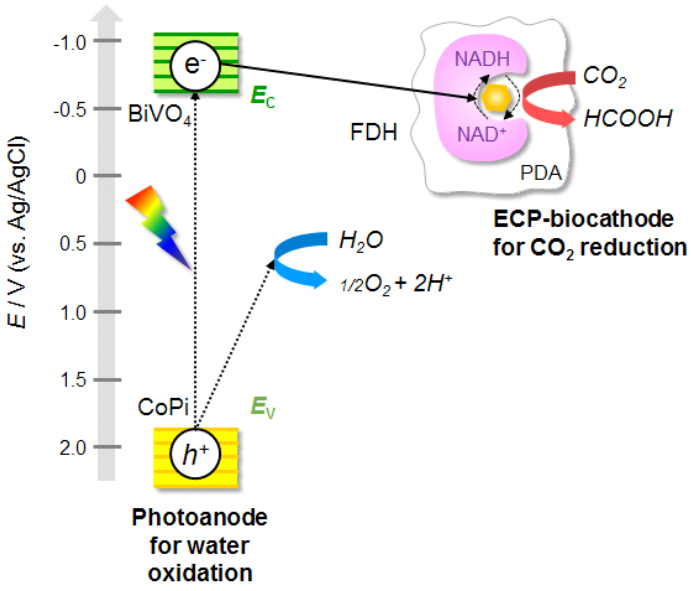

Fig. 3-23 Illustration of the functional processes underlying light-driven CO_2 reduction scheme.

Therefore, the photoanode enables to generate an electric bias under illumination similar to that of the PS II in biological photosynthesis.

3.3.4. Operation of light-driven CO_2 reduction system

The EC-PDA biocathode was functionally integrated with the $CoP_i/BiVO_4$ photoanode for water oxidation to construct a system for the selective reduction of CO_2 to formate in water without an external electrical bias (Fig. 3-24). To evaluate the performance of the self-biased CO_2 reduction system driven by light energy, current-voltage (I-V) curves with a two-electrode configuration for the EC-PDA biocathode were obtained in 0.1 M sodium phosphate buffer (pH 7.0) under constant AM 1.5 G illumination. Fig. 3-25 shows the I-V curves of the photoanodes under different conditions. The open-circuit voltage (V_{OC} at J = 0 μA cm^{-2}) was 0.47, 0.07 V (vs $CoP_i/BiVO_4$ photoanode) and the short-circuit current (J_{SC} at V = 0) was −6.41, −0.58 μA cm^{-2} under light and dark conditions, respectively. The positive V_{OC} and the negative J_{SC} for our device configuration indicate that self-biased CO_2 reduction occurred. The difference in V_{OC} between light and dark conditions allows estimation of the photovoltage: 400 mV in this system. The 110 mV and double increase in V_{OC} and J_{SC}, respectively

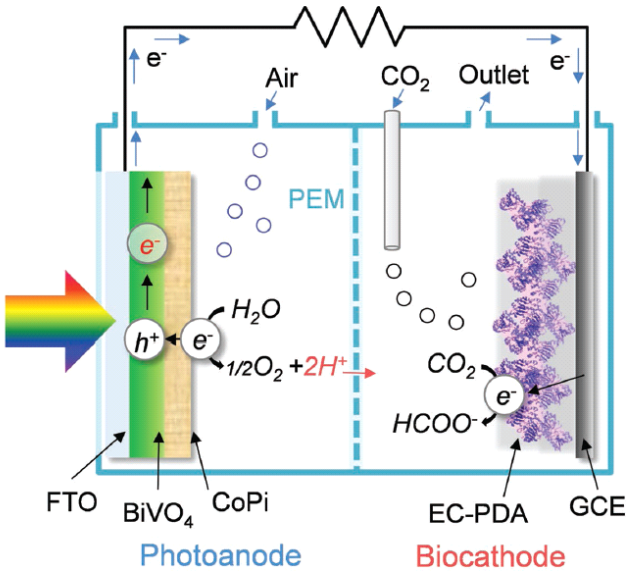

Fig. 3-24 Schematic representation of the photochemical system for the reduction of CO_2 to formate utilizing a $CoP_i/BiVO_4$ photoanode and EC-PDA biocathode working under visible light irradiation.

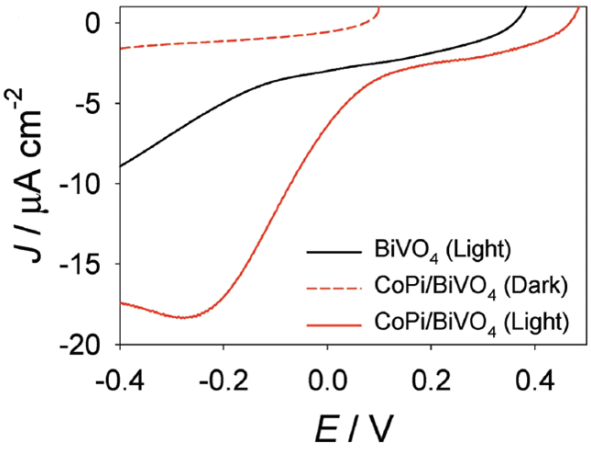

Fig. 3-25 Linear sweep voltammogram of photoelectrochemical CO_2 reduction at two-electrode configuration as shown in Fig. 3-24 (scan rate 25 mV s^{-1}).

indicate that CoP_i is a good catalyst for OER, effectively reducing the kinetic overpotential of the photoanode. For long-term stability tests, the current density was monitored for 24 h at a constant voltage of 0 V (vs $CoP_i/BiVO_4$ photoanode). The chronoamperometric current is low but stable, maintaining -0.1 μA cm^{-2}, and is believed to result from the fast kinetics at the cathode and dissolution rate of CO_2 into the aqueous solution (inset of Fig. 3-26) [7-11].

In addition, we conducted light-driven CO_2 reduction using our reactor (Fig. 3-27), and observed stable and reproducible reactivity for 24 h under constant AM 1.5 G illumination with CO_2-bubbled through the solution. Formate, the product of CO_2 reduction at EC-PDA biocathode, was analyzed by HPLC (Fig. 3-26). The amount of formate produced increased linearly with reaction time and the Faradaic efficiency determined by HPLC was 99.18 ± 6.77% at 24 h. The HPLC analysis result clearly tells that formate is only product of light-driven CO_2 reduction by the EC-PDA biocathode with almost perfect faradaic efficiency of ~100%. We calculated the conversion efficiency, 0.042%, by dividing the combustion heat of formate (270 kJ mol^{-1}) under the 1 sun illumination (100 mW cm^{-2}) [3,33,40]. The conversion efficiency is not high comparing with other abiotic combinations [41,42], but expected to be improved by simply enlarging the electrode surface area so as to increase

the total amounts of immobilized enzymes while the thickness of the enzymatic layer is unchanged.

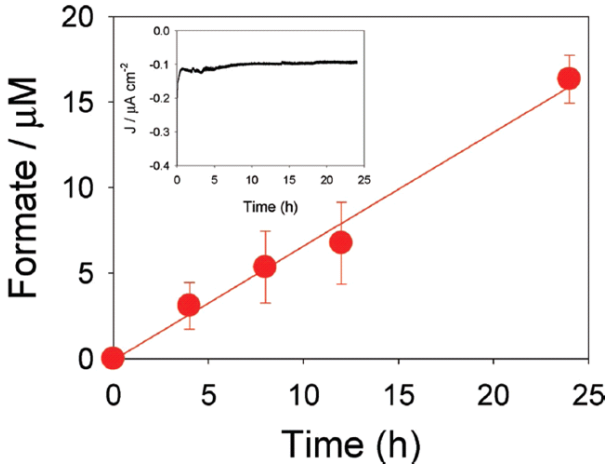

Fig. 3-26 Photocatalytic formate formation from CO_2 gas as a function of irradiation time. CO_2 reduction was performed using a two-electrode configuration with no external bias (at 0 V vs photoanode) in 0.1 M sodium phosphate (pH 7.0). The irradiation area was 1.7 cm^2 (Inset: chronoamperometry profile for 24 h).

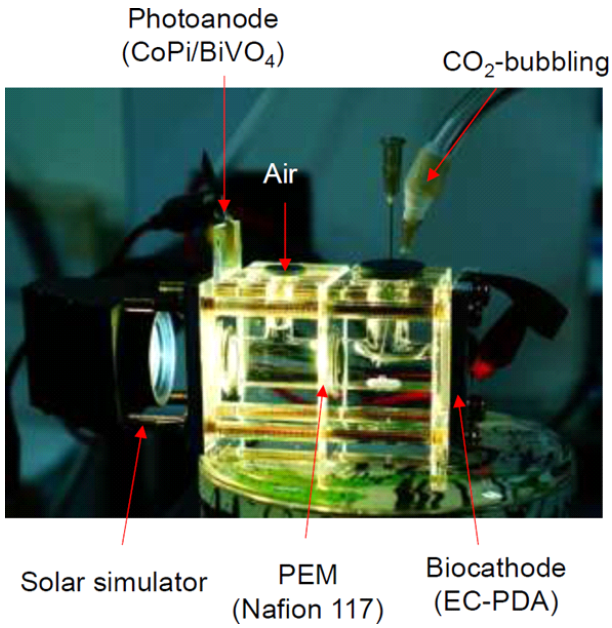

Fig. 3-27 Photograph of the photoelectrochemical system for the reduction of CO_2 to formate. The combination of a $CoP_i/BiVO_4$ photoanode and an EC-PDA biocathode functioning under visible light irradiation.

3.4 Conclusion

The thin PDA biofilm (less than 10 nm) containing FDH and NADH (EC-PDA) was electrochemically formed. Those combinations effectively enabled selective conversion of CO_2 to formate and long-lasting enzyme activity of two weeks. Although the underlying molecular mechanism of the observed phenomena in this study is still unclear so far, the counterintuitive durability of enzyme-based electrode systems are expected to originate from PDA that relays electrons between enzyme and underlying electrode through FDH and acts as an exceptional matrix for stable integration with NADH and FDH composite preventing from chronic enzyme damage. Furthermore, we have successfully produce formate spotlighted as a future hydrogen storage medium from CO_2 by integrating the $CoP_i/BiVO_4$ as a photoanode and the EC-PDA as a biocathode. By adopting combination of the well-known, low cost photoanode material and enzyme/cofactor couple, the CO_2 conversion was effectively accomplished under simulated AM 1.5 illumination with ~100% Faradaic efficiency at zero voltage. There are tremendous chances to advance the proposed system, e.g., enlarging surface area of the EC-PDA coated biocathode, optimizing band gap, band alignment and the charge

transport/transfer kinetics of photoanode, etc. The system in this study suggests a promising platform for photoelectrochemical CO_2 conversion that produces other fuels; for example, methanol and methane etc. That is because the main advantages of this system, durability and electron transfer efficiency, should be commonly valid for other kind of biofunctionalization. To do so, PDA layer needs to immobilize larger enzymes, organelles, or microbials if necessary, raising new issues to settle, e.g., affinity between PDA and biofunctional units, entrapping multienzymes, and so on.

3.5 References

[1] M. Aresta, A. Dibenedetto, A. Angelini, *Chem. Rev.*, 2014, *114*, 1709.

[2] C. W. Li, M. W. Kanan, *J. Am. Chem. Soc.*, 2012, *134*, 7231.

[3] S. Sato, T. Arai, T. Morikawa, K. Uemura, T. M. Suzuki, H. Tanaka, T. Kajino, *J. Am. Chem. Soc.*, 2011, *133*, 15240.

[4] G. Magesh, E. S. Kim, H. J. Kang, M. Banu, J. Y. Kim, J. H. Kim, J. S. Lee, *J. Mater. Chem., A* 2014, *2*, 2044.

[5] N. Kornienko, Y. Zhao, C. S. Kley, C. Zhu, D. Kim, S. Lin, C. J. Chang, O. M. Yaghi, P. Yang, *J. Am. Chem. Soc.*, 2015, *137*, 14129.

[6] G. Mohanakrishna, J. S. Seelam, K. Vanbroekhoven, D. Deepak, *Faraday Discuss,* 2015, *183*, 445.

[7] T. Reda, C. M. Plugge, N. J. Abram, J. Hirst, *Proc. Natl. Acad. Sci. U. S. A.*, 2008, *105*, 10654.

[8] A. Bassegoda, C. Madden, D. W. Wakerley, E. Reisner, J. Hirst, *J. Am. Chem. Soc.*, 2014, *137*, 4592.

[9] R. K. Yadav, J.-O. Baeg, G. H. Oh, N.-J. Park, K.-j. Kong, J. Kim, D. W. Hwang, S. K. Biswas, *J. Am. Chem. Soc.*, 2012, *134*, 11455.

[10] B. A. Parkinson, P. F. Weaver, *Nature,* 1984, *309*, 148.

[11] A. Bachmeier, S. Hall, S. W. Ragsdale, F. A. Armstrong,

J. Am. Chem. Soc., 2014, *136*, 13518.

[12] X. Wei, J. Cruz, W. Gorski, *Anal. Chem.*, 2002, *74*, 5039.

[13] M. J. Cooney, V. Svoboda, C. Lau, G. Martin, S. D. Minteer, *Energy Environ. Sci.*, 2008, *1*, 320.

[14] M. Shim, A. Javey, N. W. Shi Kam, H. Dai, *J. Am. Chem. Soc.*, 2001, *123*, 11512.

[15] R. Yuan, S. Kuwabata, H. Yoneyama, *Chem. Lett.*, 1996, *25*, 137.

[16] J. M. Laval, J. Moiroux, C. Bourdillon, *Biotechnol. Bioeng.*, 1991, *38*, 788.

[17] D. R. Dreyer, D. J. Miller, B. D. Freeman, D. R. Paul, C. W. Bielawski, *Chem. Sci.*, 2013, *4*, 3796.

[18] J. A. Seabold, K. S. Choi, *J. Am. Chem. Soc.*, 2012, *134*, 2186.

[19] J. Shi, C. Yang, S. Zhang, X. Wang, Z. Jiang, W. Zhang, X. Song, Q. Ai, C. Tian, *ACS Appl. Mater. Interfaces,* 2013, *5*, 9991.

[20] G. Loget, J. B. Wood, K. Cho, A. R. Halpern, R. M. Corn, *Anal. Chem.*, 2013, *85*, 9991.

[21] K. Kang, S. Lee, R. Kim, I. S. Choi, Y. Nam, *Angew. Chem. Int. Ed.*, 2012, *124*, 13278.

[22] N. S. Lewis, D. G. Nocera, *Proc. Natl. Acad. Sci. U. S. A.*, 2006, *103*, 15729.

[23] F. Jin, X. Zeng, J. Liu, Y. Jin, L. Wang, H. Zhong, G.

Yao, Z. Huo, *Sci. Rep.*, 2014, 4.

[24] Z. Wu, W. Jing, E. Wang, *Electrochem. Commun.*, 1999, *1*, 545.

[25] A. A. Karyakin, O. A. Bobrova, E. E. Karyakina, *J. Electroanal. Chem.*, 1995, *399*, 179.

[26] R. Castillo, M. Oliva, S. Marti, V. Moliner, *J. Phys. Chem. B*, 2008, *112*, 10012.

[27] Q. Liu, B. Yu, W. Ye, F. Zhou, *Macromol. Biosci.*, 2011, *11*, 1227.

[28] B. Yu, J. Liu, S. Liu, F. Zhou, *Chem. Commun.*, 2010, *46*, 5900.

[29] J. Liebscher, R. Mrówczyński, H. A. Scheidt, C. Filip, N. D. Hădade, R. Turcu, A. Bende, S. Beck, *Langmuir*, 2013, *29*, 10539.

[30] D. H. Nam, C. B. Park, *ChemBioChem*, 2012, *13*, 1278.

[31] B. Stöckle, D. Y. W. Ng, C. Meier, T. Paust, F. Bischoff, T. Diemant, R. J. Behm, K.-E. Gottschalk, U. Ziener, T. Weil, *Macromol. Symp.*, 2014, *346*, 73.

[32] K. Schirwitz, A. Schmidt, V. S. Lamzin, *Protein Sci.*, 2007, *16*, 1146.

[33] J. L. White, J. T. Herb, J. J. Kaczur, P. W. Majsztrik, A. B. Bocarsly, *J. CO_2 Util.*, 2014, *7*, 1.

[34] A. Bardea, E. Katz, A. F. Buckmann, I. Willner, *J. Am. Chem. Soc.*, 1997, *119*, 9114.

[35] S. R. Morrison, *Elektrochemie von Halbleitern:*

Electrochemistry at Semiconductor and Oxidized Metal Electrodes, Plenum Press, New York, 1980, p. 137.

[36] M. W. Kanan, D. G. Nocera, *Science*, 2008, *321*, 1072.

[37] B. Klahr, S. Gimenez, F. Fabregat-Santiago, J. Bisquert, T. W. Hamann, *J. Am. Chem. Soc.*, 2012, *134*, 16693.

[38] J. R. McKone, N. S. Lewis, H. B. Gray, *Chem. Mater.*, 2014, *26*, 407.

[39] T. W. Kim, K.-S. Choi, *Science*, 2014, *343*, 990.

[40] Z. Chen, T. F. Jaramillo, T. G. Deutsch, A. Kleiman-Shwarsctein, A. J. Forman, N. Gaillard, R. Garland, K. Takanabe, C. Heske, M. Sunkara, E. W. McFarland, K. Domen, E. L. Miller, J. A. Turner, H. N. Dinh, *J. Mater. Res.*, 2010, *25*, 3.

[41] T. Arai, S. Sato, T. Morikawa, *Energy Environ. Sci.*, 2015, *8*, 1998.

[42] T. Arai, S. Sato, T. Kajino, T. Morikawa, *Energy Environ. Sci.*, 2013, *6*, 1274.

4. Summary and Perspectives

This dissertation presents a study of the fabrication and design solar fuel systems by recombining already-developed catalyst materials with electrodeposition. The commercialized catalyst for solar fuel production systems has not been reported due to the lack of materials which simultaneously satisfy prerequisites of efficiency, stability, and cost-effectiveness. Although numerous researches have been focused on the development of new catalyst material, Pt group-based elements are still the optimum materials, which suffer from high cost and price instability. We sought another breakthrough by attempting to design and electrodeposit well-known, non-precious catalyst, e.g., changing morphology in micro-scale and recombining with insertion of conductive molecular scaffolds.

For efficient PEC hydrogen production, the development of transparent catalysts for minimizing the optical losses originating from scattering and/or absorption by the catalyst is an emerging issue. In **Chapter 2**, the direct electrodeposition of patterned NiMo, a well-known non-noble catalyst for hydrogen production, was carried out by illuminating with patterned light using a digital micromirror device (DMD). This process was completed in a single step without any mask. Such patterned NiMo/a-Si

photoelectrodes with sufficient catalyst loading have a bare surface that allows light transmission, resulting in the intrinsic saturated current density and photovoltage of the a-Si. Moreover, long-distance lateral electron transport between the adjacent NiMo catalyst patterns was observed. Based on the results, this strategy could be applied to the fabrication of a-Si based heterojunction photocathode with higher efficiency. We believe that the proposed maskless electrodeposition technology is a significant step towards developing a practical solar light-driven water splitting system.

The electrochemical conversion of CO_2 to chemical fuels has attracted considerable attention. Among the many approaches, exploiting and mimicking biocatalytic components is a promising method because of their powerful catalytic ability, which is rarely achievable with artificial, inorganic catalysts. In Chapter 3, the electrode for CO_2 reduction to formate was prepared by the single-step electropolymerization of dopamine in the presence of a FDH to transform CO_2 to formate and the NADH that mediates electron transfer between the underlying electrode and the reaction center in FDH. As a result, a PDA thin film with a thickness of ca. 10 nm enclosing FDH and NADH was deposited on a glassy carbon electrode. At this artificial bioelectrode, the conversion of CO_2 to formate occurred at

comparatively low potentials (−0.4 V vs. Ag/AgCl at pH 7.0) and a Faradaic efficiency of 99.18 ± 6.77% was achieved. In addition, this thin−film bioelectrode showed a prolonged catalytic enzyme activity of approximately two weeks. This long−term stability was far from expectations because the characteristics of artificial biological systems suffer from intrinsic vulnerability. Although the precise working principles of the system have not been discovered, it is expected that the intimate chemical communication between the polydopamine, FDH and NADH is a key factor. The production of formate from CO_2 took place at zero voltage under simulated AM 1.5 illumination because the potential of the conduction band of $BiVO_4$ was slightly negative than the redox potential of NADH at neutral pH and the biocathode converts CO_2 with a minimal overpotential.

In line with the aforementioned researches, further studies are required in the following areas: the effect of patterning a three−dimensional, nano−sized electrocatalyst onto PEC energy conversion system, the electron transfer mechanism from the substrate electrode to the reaction center in the enzyme through the PDA−based structure, and facile design of the combination of a bioelectrode with a semiconductor by mimicking artificial photosynthesis. Furthermore, in−depth studies on the semiconductor electrochemistry investigating the electrolyte/catalyst/semiconductor interface. The

influence of various conditions of PEC cells on typical macro-scale electrochemistry, e.g. cyclic/linear sweep voltammograms and electrochemical impedance spectroscopy, have frequently been reported. However, as shown in our researches, changes in micro- or nano-scale morphology or molecular structure brought entirely new results for solar fuel production on photoelectrodes. Hence, it is worth studying the progress of *in situ* electrochemical reactions in small spatial dimensions, viz. micro- or nano-scale, and on short time scales. Even on heterogeneous surfaces with nano- or atomic scale morphology, crystal orientations, defect sites, and chemical compositions have reportedly brought about considerable changes in macro-scale results, but rigorous chemical analysis has not been carried out so far. Elucidating those factors with small spatial and temporal resolutions will lead to an improved understanding of the PEC energy production systems and to better design of PEC cells.

국문초록

화석 연료의 무분별한 사용으로 환경오염에 대한 문제가 사회적 이슈로 대두되고 있다. 하지만 이에 반해 에너지에 대한 수요는 해마다 늘어만 가고 있어 화석 연료를 대체할 청정 에너지원에 대한 기술 개발이 시급한 실정이다. 여러 가지 후보 기술 중 가장 촉망받는 기술 중 하나는 광전기화학 반응을 이용해 태양 에너지를 분자 내 화학 결합 에너지에 저장을 하는 기술이다. 이와 같은 태양 연료 생산을 위해 1970 년대 이후로 광전기화학셀에 관한 연구가 많이 이루어져 왔다. 광전기화학셀은 주로 광반도체 전극, 분리막, 촉매로 구성된다. 그 중 촉매 분야에서는 성능이 뛰어나고 경제적이면서도 안정한 촉매의 개발이 필요하다. 이러한 조건을 만족시키는 촉매를 찾기 위한 현재까지 대부분의 연구는 새로운 촉매 물질을 개발하는 것에 초점이 맞춰져 있다. 과거 상용화를 할 수 있는 촉매 개발에 대한 수많은 시도가 있었음에도 불구하고 태양 연료 생산 기술에 실제로 적용할 수 있는 촉매 물질 개발은 현재까지 성공한 사례가 없다. 상용화에 실패한 가장 큰 원인 중 하나는 경제성을 얻기 위한 효율과 생산 단가 사이의 괴리를 없애줄 수 있는 물질이 아직까지 개발되지 않았기 때문이다. 본 학위 논문은 태양 연료 생산을 위한 촉매 연구 중 주류를 이루고 있는 물질 개발 연구에 한 발짝 물러나서, 경제적인 용액 기반 공정을 통해 만들어질 수 있다고 알려진 촉매 물질로 전극을 새롭게 구성해 성능 개선 향상에 성공한 두 가지 연구 사례를 포함하고 있다. 이러한 연구는 새로운 촉매 물질 개발에만 몰두할 것이 아니라 알려진 촉매 물질을 통해 광전기화학 인터페이스에 대한 보다 근원적이고 기초적인 연구가 필요하다는

시사점을 안겨 줄 수 있다고 여겨진다.

첫째, 비정질 실리콘의 광전도성을 이용해 촉매 물질을 표면에 직접 패터닝을 할 수 있는 광-유도 전기 도금법을 개발했다. 이 전기 도금 기술을 사용하여 디지털 미소 반사기를 통해 만들어진 패턴된 광원과 동일한 모양의 니켈-몰리브데넘 합금 촉매를 비정질 실리콘 표면에 패터닝했다. 니켈-몰리브데넘 합금 촉매는 수소 발생 촉매로 널리 알려져 있는 물질이다. 이러한 패터닝 과정은 통상적인 포토리소그래피에서 사용하는 필름 마스크와 복잡한 여러 단계의 필수 과정 없이 단일 과정으로만 이뤄질 수 있다. 이렇게 패턴된 니켈-몰리브데넘 패턴/실리콘 산화막/비정질 실리콘 광전극은 충분한 양의 니켈-몰리브데넘 촉매를 표면에 위치시키면서도 동시에 빛이 패턴된 촉매 사이의 비정질 실리콘 표면으로 잘 투과할 수 있게 할 수 있었다. 그 결과, 비정질 실리콘 자체의 전류밀도 (0 V vs. RHE) 와 광전압을 유지할 수 있었다. 더불어 전자들이 패턴된 촉매 사이로 표면을 통해 비정질 실리콘에서 알려진 전자의 확산 거리보다 길게 이동할 수 있음을 밝혔다.

두 번째로 생체 시스템을 모방하여 이산화탄소를 포름산염으로 광변환할 수 있는 전극을 개발했다. 포름산염은 수소를 액체 형태로 저장할 수 있는 매질로서 촉망받는 물질 중 하나이다. 이산화탄소 환원이 일어나는 환원 전극은 바이오 촉매 역할을 하는 formate dehydrogenase (FDH) 와 전자 전달 매개체 역할을 하는 nicotinamide adenine dinucleotide (NADH) 가 도금 용액에 함께 존재하는 상태에서 dopamine 산화를 통한 polydopamine (PDA)

폴리머 중합 전기 도금을 통해 만들어졌다. 이렇게 해서 만들어진 환원 전극을 cobalt phosphate (CoP_i) 산소 발생 촉매가 입혀진 bismuth vanadate ($BiVO_4$) 광산화 전극과 연결시켜 이산화탄소 환원의 상대 전극으로서 전류가 순환할 수 있는 시스템을 만들었다. FDH 의 뛰어난 촉매 활성과 뼈대와 동시에 전도성 와이어 역할을 하는 PDA, 충분한 광전압을 제공하는 $CoP_i/BiVO_4$ 덕분에, 외부 전압이 인가되지 않는 상태에서 시뮬레이션된 태양광만을 가지고도 이산화탄소를 광화학 반응을 이용해 포름산염으로 변환할 수 있었다.

주요여: 광전기화학셀, 촉매, 광-유도 전기도금법, 수소 발생, 이산화탄소, 폴리도파민, 폴리머 전기중합법

학번: 2009-22918